4-21-2022 9:00 AM

The Application of Digital Volume Correlation Bone Strain Measurements in the Osteoarthritic Glenohumeral Joint

Jakub R. Targosinski, *The University of Western Ontario*

Supervisor: Ferreira, Louis, *The University of Western Ontario*
A thesis submitted in partial fulfillment of the requirements for the Master of Engineering
Science degree in Biomedical Engineering
© Jakub R. Targosinski 2022

Abstract

This thesis investigates the accuracy and precision of digital volume correlation measurements derived from micro-computed tomography imagery of interfaces in the upper extremity of clinical relevance, namely, the implant-cement-bone interface of glenoid implants used in total shoulder arthroplasties and the implant-bone interface of shoulder hemiarthroplasties. The works within derive relationships between measurement accuracy and precision and parameters of practical interest such as image quality and measurement spatial resolution. It also analyzes the effects of micro-computed tomography image artifact-inducing materials on the accuracy and precision of digital volume correlation-based measurements. The spatial relationship between distance between the artifact-inducing material and the magnitude of change in accuracy and precision is also investigated. Finally, it also contains an *in vitro* model of the peripheral glenoid peg-cement-bone interface which is subsequently analyzed through digital volume correlation; the relationship between peg/bone region and strain magnitude is elucidated.

Keywords

Summary for Lay Audience

Shoulder osteoarthritis can be a debilitating disease that afflicts two-thirds of individuals older than 65. Current surgical treatments of shoulder osteoarthritis include partial and total shoulder replacements. The implants and/or bone in these shoulder replacement procedures face longevity challenges post-surgery when compared to other joint replacement procedures such as hip replacements or knee replacements, and typically require revision surgery much sooner than is desirable. In order to analyze the manner of failure of these implants, imaging techniques such as high-resolution CT imagery can be used to investigate simulated models of these critical surgical procedures. High-resolution CT imagery can be captured of the bone, implant and implant fixation in both a relaxed state and a state that reflects what the shoulder experiences while under load. These images can then be compared to one another in order to determine the deformation of the bone, the implant fixation, and the implant itself. This measurement technique, known as digital volume correlation, can be used to analyze a variety of clinically relevant problems in the shoulder post-shoulder replacement. However, the magnitude of measurement error associated with digital volume correlation measurements in this application are not well understood and must be first quantified prior to investigating the aforementioned clinical problems. This thesis investigates the accuracy and precision of digital volume correlation measurements in the context of certain shoulder implants and bone configurations in order to prepare for future models which leverage digital volume correlation to study these shoulder implants. It also conducts an analysis of a specific location of one of these shoulder implants which is of potential interest in terms of explaining the early failure of these implant systems. This thesis finds that the accuracy and precision of digital volume correlation measurements are sufficient to investigate the aforementioned clinical problems. The model analysed in this thesis also reinforces the suggestion that the specific location investigated in the shoulder implant is of high interest and could be a reason for the early failure of these implants.

Co-Authorship Statement

Chapter 1

J Targosinski-sole author

Chapter 2

J Targosinski-data collection, statistical analysis, digital volume correlation analysis, manuscript author, study design

J Kusins-edited manuscript, study design, data collection

L Ferreira-study design, edited manuscript

N Martensson-data collection, statistical analysis

A Nelson-data collection

N Knowles-study design

Chapter 3

J Targosinski-data collection, statistical analysis, digital volume correlation analysis, manuscript author, study design

J Kusins-edited manuscript, study design, data collection

L Ferreira-edited manuscript, study design

Chapter 4

J Targosinski-data collection, statistical analysis, digital volume correlation analysis, manuscript author, study design, instrumentation design

J Kusins-study design

L Ferreira-study design, edited manuscript

A Nelson-data collection

Chapter 5

J Targosinski-sole author

Acknowledgments

To my friends and family for standing by me throughout the whirlwind of the past two years I thank you. It's been a difficult time for us all, and I'd like to recognize that (and hopefully preserve a memory of this permanently to some extent) in the dusty annals of the thesis repository (though I suppose it's a dusty server stack which preserves the digital version). Your support, love and affection have been my bastion to fall back on.

To the members of the HULC lab with whom I've had a fantastic experience: the mentorship and guidance that you've provided have been central to this work; without it the pen would have never made it to paper here. Jon, Corey, David, Moe, Cintya, Nik—thank you all for all your help! To my supervisor, Dr Ferreira, I extend a particular thank you and overwhelming sense of appreciation—your unending patience and understanding have made it possible for me to make it to the finish line.

Finally, a sentiment that I want to include: to the things we lose along the way. A journey is naught without a precarious balance of loss and gain.

Nomenclature

ε	Strain
μ	Micro
2D	Two-dimensional
3D	Three-dimensional
BV/TV	Bone volume/total volume
CT	Computed tomography
DVC	Digital volume correlation
DOF	Degrees of freedom
HA	Hydroxyapatite
MAE	Mean absolute error
OA	Osteoarthritis
SHA	Shoulder hemiarthroplasty
SDE	Standard deviation of error
TB.N.	Trabecular number
Tb.Sp.	Trabecular separation
Tb.Th.	Trabecular thickness
TSA	Total shoulder arthroplasty
GHJ	Glenohumeral joint

Table of Contents

List of Tables

List of Figures

1   Introduction

OVERVIEW

This chapter introduces the relevant concepts that are investigated in this thesis. An overview of the macro- and microscopic anatomy and physiology of the glenohumeral joint is provided, followed by a discussion of current clinical problems and the corresponding treatments that are present in this important biomechanical interface. In the pursuit of improving these clinical treatments the biomechanics of the underlying problems must be well-understood; current approaches to investigating the biomechanics of these problems are introduced, followed by the rationale and objectives of this thesis and how digital volume correlation in combination with micro-CT imagery is employed in order to investigate critical aspects of these problems.

1.1   Glenohumeral Anatomy

The glenohumeral joint of the human shoulder is a synovial ball-and-socket joint that consists of the interface of the humerus and glenoid fossa of the scapula.[1,2] It is the most mobile joint of the human body, sacrificing stability for mobility in order to achieve its large range of motion.[1,2] To enable this highly specialized compromise, the articular surface of the scapula—the glenoid fossa—is flatter than other comparable synovial joints such as the femoroacetabular joint of the hip, and the joint itself is stabilized by a complex interaction between the constituent ligaments, muscles and the underlying bone.[3,4] The ligaments, such as the superior, middle and inferior glenohumeral ligaments, provide passive stability and the muscles, such as the supraspinatus, deltoid and subscapularis provide dynamic stability during motion.[3,4]

A common pathology of the glenohumeral joint is the osteoarthritic degradation of the interface through progressive damage to the chondral and osseous tissues of the humerus and glenoid.[5,6] The pathogenesis of osteoarthritis is somewhat understood and is described in detail below, but in order to contextualize that explanation, the nature of the osseous tissues that experience the disease must also be expounded upon.

1.2 Bone

Bone is a complex, dynamic material that is composed of multiple primary and emergent elements that are organized on a wide range of hierarchies of scale.[7] The fundamental constituents of bone are type I collagen, a ubiquitously occurring connective tissue protein in human connective tissue which comprises approximately 30% of the human body by protein content, carbonate-substituted hydroxyapatite (HA) or hydroxyapatite-like compounds, and water.[8] These three materials, which exist on a length scale of nanometers, are then organized into mineralized collagen fibrils, in which parallel fibers of collagen suspend a crystal of hydroxyapatite.[7,9] The individual mineralized collagen fibrils are then woven in multiple patterns into fibril arrays, which subsequently become the lamellae of cortical bone. The lamellae organize into sheets and osteons, which finally give rise to the macroscopic structure of bone. [7–9]The dynamic aspect of bone refers to its ability to continuously remodel based on physiologically experienced loads: bone remodeling is a complex control system meditated primarily by three distinct cell types: osteoclasts, which resorb bone, osteoblasts, which synthesize new bone, and osteocytes, which are embedded in the bony matrix and transduce loads.[8] Osteocytes transduce bone loads through deformation of the rigid extracellular matrix in which they are embedded and subsequently signal osteoclasts and osteoblasts to remodel bone based on the experienced loads.[8] As the primary structural element of the human body, the ability of bone to self-repair and dynamically adapt to experienced loads is paramount to its role—bone is constantly remodeling, restructuring and repairing itself in order to serve its physiological purpose. [8]
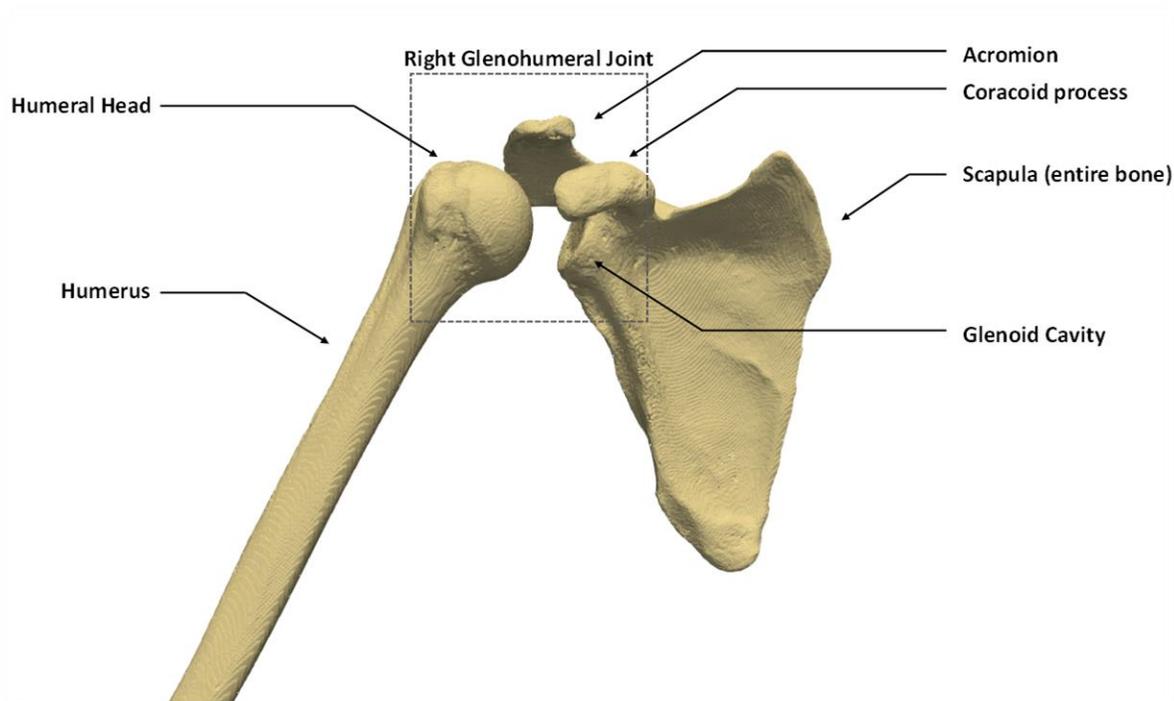
Figure 1: Skeletal components of the right glenohumeral joint as isolated from clinical CT imagery of a cadaveric specimen.

1.3 Osteoarthritis

The intricate control system which governs bone remodeling is susceptible to dysregulation. The most prevalent pathology in which this occurs is osteoarthritis, a debilitating disease which progressively damages bone and which affects approximately two-thirds of people older than 65 years.[5,10] The hallmarks of osteoarthritis (OA) are otherwise idiopathic joint pain which upon further examination through medical imaging is revealed to be caused by macroscopic changes and damage in the tissues of joints responsible for load transfer.[5,10] Foremost amongst osteoarthritic presentation is the degradation and eventual total loss of chondral tissues that rest atop bone and facilitate frictionless motion and shock absorbance at the joint interface. Other markers are the presence of osteophytes (or bone spurs) which indicate substantial bone remodeling is occurring in the boney tissues of the joint.[5,10,11] The pathogenesis of osteoarthritis may potentially begin with subclinical inflammation of the synovium of cartilage, or local trauma to the chondral tissue.[5] This initial inflammation, combined with other risk

factors, such as genetic predisposition and the long-term mechanical loading characteristics of the joint lead to a positive feedback loop of resorption of the chondral extracellular matrix. Crosstalk/cell signaling between the chondral tissues and the subchondral bone leads to an increase in stiffness in the subchondral bone, which causes mechanical damage to the cartilaginous tissue; this in turn drives more debilitating mechanical changes in the underlying bone. This process ultimately erodes the chondral tissue and exposes the subchondral bone.

1.4   Clinical Treatment of Glenohumeral Osteoarthritis

In the glenohumeral joint, end-stage osteoarthritis can be treated with total shoulder arthroplasty (TSA): a procedure which resects the humeral head and replaces it with a compatible implant material (typically a biocompatible ceramic or metallic alloy, though more exotic composite solutions are a topic of active research and development).[12,13] The surface of the glenoid fossa is also replaced with an ultra-high molecular weight polyethylene (UHMWPE) glenoid implant that acts as a new articulating surface for the implant humeral head.[12] These glenoid implants can be cemented, meaning they incorporate polymethyl-methacrylate (PMMA) orthopedic bone cement in their fixation in the bone underneath the glenoid fossa, or cementless, meaning they rely on natural bone ingrowth and remodeling for their fixation strength.[12] In the context of glenohumeral osteoarthritis treatment, the patient population typically receives a cemented bone implant as expectations of bone ingrowth and remodeling are generally poor in older individuals and therefore cementless implants are contraindicated. Total shoulder arthroplasty generally has positive outcomes: patients report increases in mobility, decreases in pain, and a general restoration of some degree of normal joint function.[12] However, the treatment is not without its shortcomings: revision surgery after TSA occurs more often and sooner than in other comparable joint arthroplasties such as those of the knee and hip.[14–16] The most common cause of revision is the symptomatic loosening of the glenoid implant—meaning the cemented fixation has failed and the implant has become mobile within the bone of the scapula.[17,18] Fixation of implants in the glenoidal space is complicated in patients with osteoarthritis as the quality and volume of bone available for fixation is typically very low.[19] Moreover, the natural anatomical

features of the glenoid and scapula do not make matters easier: the glenoid has a very small surface area and the scapular process behind the glenoid quickly narrows, creating a very small anatomic space in which the implant fixation can reside.[12] Contrasted with the large articular surface of the acetabulum and the bone volume available in the pelvis in total hip arthroplasty, it is no surprise that the fixation of the glenoid implant is lasts a comparatively shorter amount of time *in vivo* than that of an acetabular cup implant. Improving the long-term survivability of the fixation of the glenoid implant is contingent on understanding the mechanical properties of the trabecular bone under the glenoid fossa and the interaction of this bone with the cement mantle of the implant.

An alternative surgical treatment for glenohumeral osteoarthritis is shoulder hemiarthroplasty (SHA).[6] This revision involves the partial replacement of the articulating components of the glenohumeral joint: the humeral head is resected and replaced with an implant humeral head, and the glenoid surface is left unaltered. This surgical approach to treatment of glenohumeral OA has declined in popularity due to poor outcomes relative to TSA, but recent research into alternative humeral head implant materials which aim to assuage the shortcomings of SHA have revived interest in its feasibility.[6,13,20] Investigations into these materials continue and are reliant on an understanding of the mechanical properties of the articular surface and the subchondral bone.[13,21,22]

Total Shoulder Arthroplasty

Humeral Head Implant   Glenoid Implant   Humeral Head Implant

Glenoid Implant

Shoulder Hemiarthroplasty

Humeral Head Implant   Humeral Head Implant
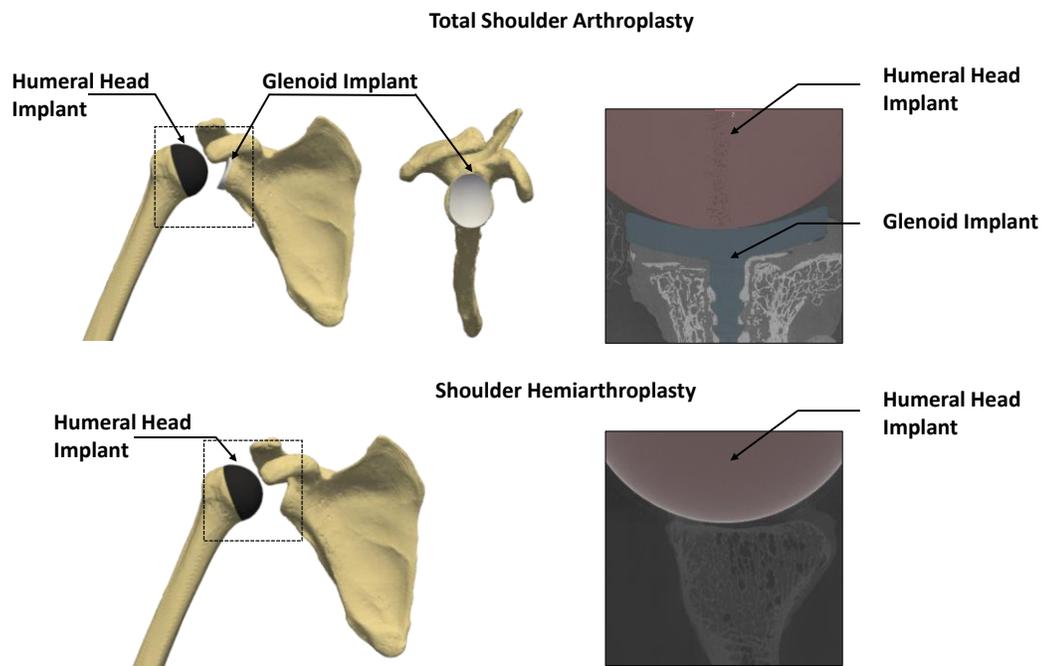
Figure 2: Anatomic components and implants of total shoulder arthroplasty (top) and shoulder hemiarthroplasty (bottom). Micro-CT imagery (isotropic voxel size: 33.5µm) of cadaveric models of both interfaces are shown on the right.

1.5   Biomechanical Role and Properties of Trabecular Bone

At macroscopic length scales, two readily apparent classes of bone can be defined: cortical (or compact) bone, which constitutes the outer shell of bone, and spongy (or cancellous/trabecular) bone, which is present in the interior of bone primarily at the end of long bones or underneath areas of high load transfer such as in vertebral bodies.[7,8,23,24] As the name "spongy" implies, cancellous bone is made of a porous and foam-like network of constituent elements referred to as trabeculae. Its biomechanical role is to enable load transfer from joints to the cortical bone of the cortex of long bones, or to the cortical bone of vertebral bodies.[25] Trabecular bone is an anisotropic and heterogenous material that is composed of both stiff and elastic tissues: the relatively hard rods of the trabeculae compose a lattice that is embedded with highly cellularized marrow, forming a bulk structure that is highly ductile relative to cortical bone.[23] On the local scale, the mechanical properties of trabecular bone are driven by two factors: degree of

mineralization and collagen content. At the apparent scale, the constant remodeling of bone trabeculae, as well as the complexity of the anisotropic trabecular matrix, cause difficulty in quantifying the mechanical properties of trabecular tissue.[23,24] Trabecular bone has lower calcium content and tissue density than cortical bone. As trabecular bone is an important force propagator, it is more active in remodeling than cortical bone, and as different anatomic sites transfer different loads, trabecular bone can vary highly between anatomic site.[26,27] In order to quantify the structural parameters upon which this variation depends, morphometric parameters which describe certain features of trabecular bone have been developed which describe different elements of the heterogeneity of the trabecular network.[28,29] Typically these parameters describe identifiable geometric aspects of the trabecular network as seen through volumetric imagery.[28,29] In particular, high-resolution computed tomography imagery developed from x-ray or synchrotron light sources have both been used to investigate the trabecular network.[30,31] Morphometric parameters such as bone volume/total volume (BV/TV), a measure of the proportion of the image occupied by the trabecular structure, trabecular thickness (Tb. Th.), the apparent mean thickness of the trabeculae, trabecular separation (Tb. Sp.), the mean distance between trabeculae, and trabecular number (Tb. N.) a measure of the one-dimensional density of trabeculae in the trabeculae network are all commonly reported in the literature as a means of quantifying and controlling for the heterogeneity of trabecular bone.[28,29] Other morphometric parameters exist to quantify the anisotropic properties of trabecular bone, but they are outside the scope of this thesis.
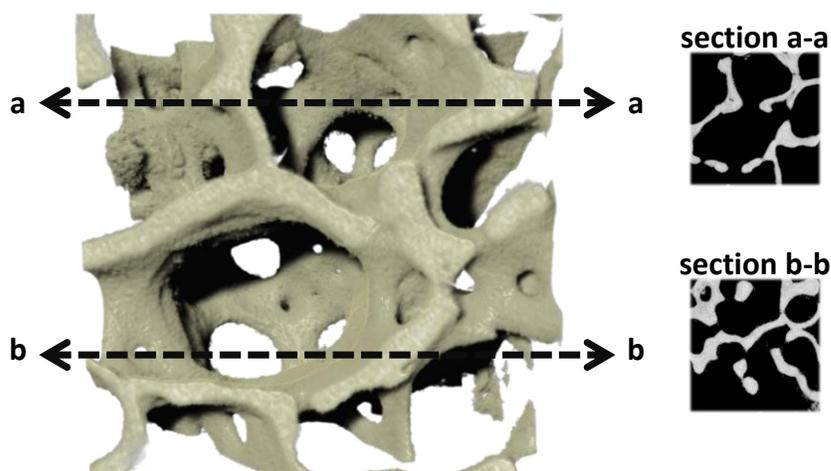
Figure 3: 3D model of trabecular structure isolated from micro-CT imagery. (Isotropic voxel size: 12 µm)

1.6 *In vitro* Mechanical Testing of Bone

Translating the mechanical behaviour of bone from tissue-level properties to gross explanations of clinically relevant problems remains a challenge. *In vivo* mechanical micro-scale resolution testing of bone is approaching the realm of possibility, with high resolution peripheral quantitative computed tomography approaching spatial resolutions on the order of 100 µm in real time in clinical settings, but currently the standard for mechanical testing of bone revolves around *in vitro* cadaveric models or in-silico FE models.[32] Within the scope of this thesis, only *in vitro* cadaveric testing will be discussed. *In vitro* models of bone deformation typically employ cadaveric osseous tissues in order to closely replicate the mechanical properties of native bone.[33–35] The use of cadaveric tissues in mechanical testing imposes a strict set of limitations to the translatability of the knowledge gleaned from these models: cadaveric bone is static, i.e. does not remodel as a function of load as native tissue does; the inclusion of soft tissues that exist *in vivo* may be difficult to control in cadaveric models, and *in vivo* loading parameters of joints and other anatomic constructs are still not entirely understood so applying relevant loads to cadaveric models can be difficult.[33–35] There is still substantial value in testing cadaveric tissue, however, as critical mechanical aspects of the tissue are preserved from their *invivo* state.[33–35]

Recent developments in the mechanical testing of cadaveric bone tissues have centered around the integration of 6-DOF Stewart platforms into mechanical testing methodologies.[36,37] The Stewart platform uses six prismatic actuators attached in pairs to three positions on the base plate which are then attached anti-modally to a top plate. The connections between the actuators and base and top plate are made with universal joints. This configuration allows for 6 degrees of freedom in motion; the configuration also ensures that the actuators only experience linear loads which allows for high load generation. The relative inexpense of these robots as compared to purpose-built joint simulators and their versatility and adaptability to multiple applications and simulations makes them advantageously positioned to other *in vitro* mechanical testing devices.[37]
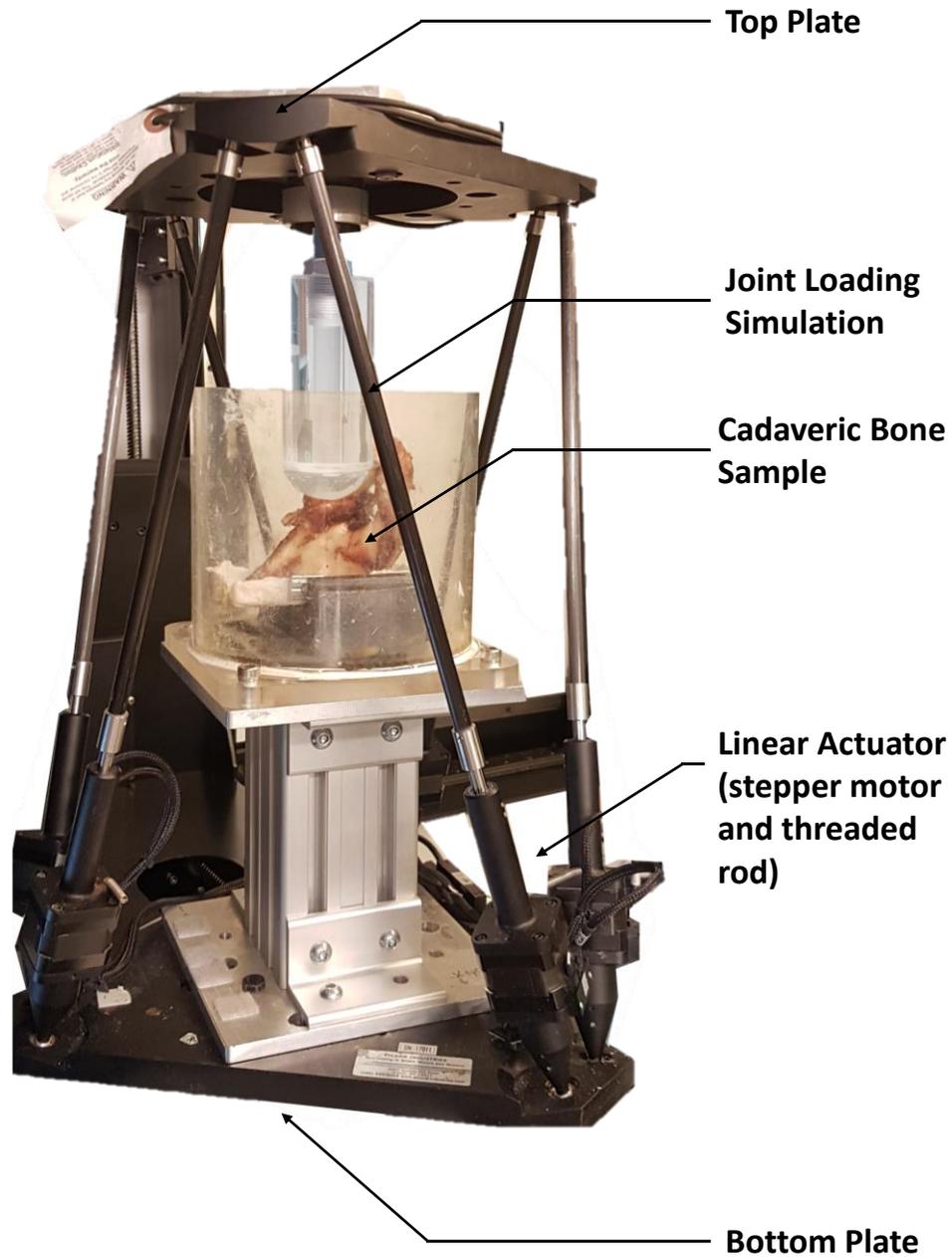
Figure 4: An example of an application of a Stewart platform to perform biomechanical testing of bone. Components critical to the function of a Stewart platform are labelled.

1.7 Strain Measurement Methodologies in Bone

A common outcome measure in biomechanical testing of bone is bone strain. At the apparent level, bone strain can predict global fracture failure in bone. At both the local and apparent level, bone strain can potentially predict sites of interest for bone remodeling. Multiple experimental biomechanical bone strain measurement methodologies exist; of note are strain gauges, digital image correlation and digital volume correlation.[38]

Strain gauges are simple deformation transducers that can be attached to discrete locations on the cortical shell of bone in order to measure the local strain. As the bone deforms, the resistance of the internally oriented wire varies in proportion to the elongation of the gauge. As the gauge electrical and geometric properties are known, the corresponding voltage change can be converted to a strain measurement. A critical limitation of strain gauges is their inability to measure internal strains; strain gauges cannot be placed within bone in order to measure trabecular strains. Typical approaches employing strain gauges use them either in combination with another measurement technique and/or at known critical locations on the surface of bone.[39,40] Attempts to establish relationships between surface strains and internal bone strains have been made, however, the internal behaviour of bone is only loosely correlated with surface strains and therefore the application of strain gauges is limited to discrete cortical strains.[41]

Digital image correlation can measure full-field surface strains of loaded bone specimens. By applying a heterogenous pattern to the surface of a bone specimen prior to mechanical testing and subsequently capturing images in an unloaded and loaded state, surface strains on the bone can be measured by differentiating local displacements in the heterogenous pattern visible in the images.[42] Like strain gauges, DIC is limited to surface measurements, and is not suitable for quantifying internal behaviour of bone.[42]

The 3-dimensional extension of digital image correlation is digital volume correlation. Digital volume correlation leverages the heterogenous, deformable internal structures of bone to perform the same function as the heterogenous surface pattern in digital image correlation.[36,43–47] Through high-resolution volumetric imagery, such as those enabled

through x-ray micro-CT or other imaging modalities, images can be captured of the internal structures of bone in an undeformed and deformed state. Digital volume correlation can then calculate the full-field displacements between the images, and those displacements can be differentiated into full-field strains. A significant disadvantage of DVC is the high resolution volumetric imagery required: with current imaging technology, the compromise between acquisition time, image quality and image resolution is an important consideration. Acquisition times can be long, but imaging technology is continuously developing and the DVC approach becomes more attractive as the compromise between acquisition time and imaging resolution becomes more favourable as a result of technological advances.

1.8   Digital Volume Correlation and Volumetric Imagery

As previously mentioned, high resolution volumetric imagery is fundamental to a DVC-based strain measurement methodology. As all volumetric imagery utilized within this thesis is micro-CT based imagery, the scope of the thesis will be limited to discussions thereof. Micro-CT imagery is generated through measurements of the attenuation of a generated x-ray beam of known intensity after it has passed through a volume of interest. Through the use of a rotating stage or rotating source, multiple attenuated x-ray projections are captured of the volume of interest. The amount of projections captured positively influence image quality, but also increase acquisition time. The projections are then used to reconstruct the volume of interest through an image reconstruction algorithm that combines the spatial information contained in each attenuated x-ray measured at the CT sensor.[48]

The images captured through micro-CT imagery can have resolutions as low as 5 µm.[49] As the length scale of bone trabeculae vary, but are typically on the order of 100um, the structure of the trabecular matrix is correspondingly captured in great detail in micro-CT imagery.[32] By combining a mechanical testing protocol and micro-CT imagery, the internal deformation of bone can be used to drive a DVC measurement approach. DVC approaches can be either local—that is, the DVC algorithm segments the volumetric image into constituent sub-volumes and calculates displacements for each sub-volume independently, or global—where distinct nodes in the image are chosen for vector

locations, but the entire image is considered in the generation of the displacement vectors.[44] The full-field displacements derived from each of these approaches are then differentiated into strains. Both of these approaches rely on establishing a correlation coefficient for the image comparisons (Eq 1. is a normalized correlation coefficient, which is well-suited for correlating images with lighting intensity fluctuations):

$$Eq.\,1,\, C_{norm}(dx, dy, dz) = \sum_{(i,j,k)} \frac{(A_{i,j,k} - \langle A \rangle)(B_{i+dx,j+dy,k+dz} - \langle B_{dx,dy,dz} \rangle)}{\sqrt{|A'|^2}\sqrt{\left|B'_{dx,dy,dz}\right|^2}}$$

Where $A_{i,j,k}$ is the gray value intensity at the voxel position i, j, k in volume A and $B_{i+dx,j+dy,k+dz}$ is the gray value intensity in volume B at the position shifted by dx, dy, dz. This correlation value is maximal when the true displacement solution is found.

The sub-volume size in local DVC (the approach used in this thesis) is equivalent to the spatial resolution of the strain and displacement measurement made. There is an inherent trade-off made between increasing the spatial resolution of the local DVC measurement and the quality of the correlations being made. As the spatial resolution increases, the amount of information available to construct a non-spurious correlation correspondingly decreases. Therefore, there is an important balancing act in using a spatial resolution that is acceptable for the purposes of the measurements to be made and maintaining the integrity of the DVC analysis performed. Many methods in the literature exist to analyze this relationship: of note are the zero-strain method and the virtual deformation method. In the zero-strain method, two undeformed images are captured and correlated with one another. The relationship between the mean absolute error, standard deviation of error and spatial resolution of the measurement are examined, and a value of error and spatial resolution that are acceptable to the user are selected for further analysis of deformed images. In the virtual deformation method, a known affine transformation is applied to the image, and the difference between the known transformation matrix and the measured displacements is calculated. A relationship between the relative error and spatial resolution is again constructed and a compromise is reached with respect to the measurement error and spatial resolution.[50] Both of these approaches are viable methods

of quantifying the DVC measurement accuracy and precision. A commercially available software, DaVis-DVC, is used in this thesis to perform digital volume correlation strain measurements. DaVis-DVC implements a multiple pass approach to DVC to improve analysis speed and accuracy. A first pass is made through an FFT approach (FFT-DVC) to generate a predictor field, then subsequent passes as specified by the user implement a direct (DC-DVC) correlation approach.
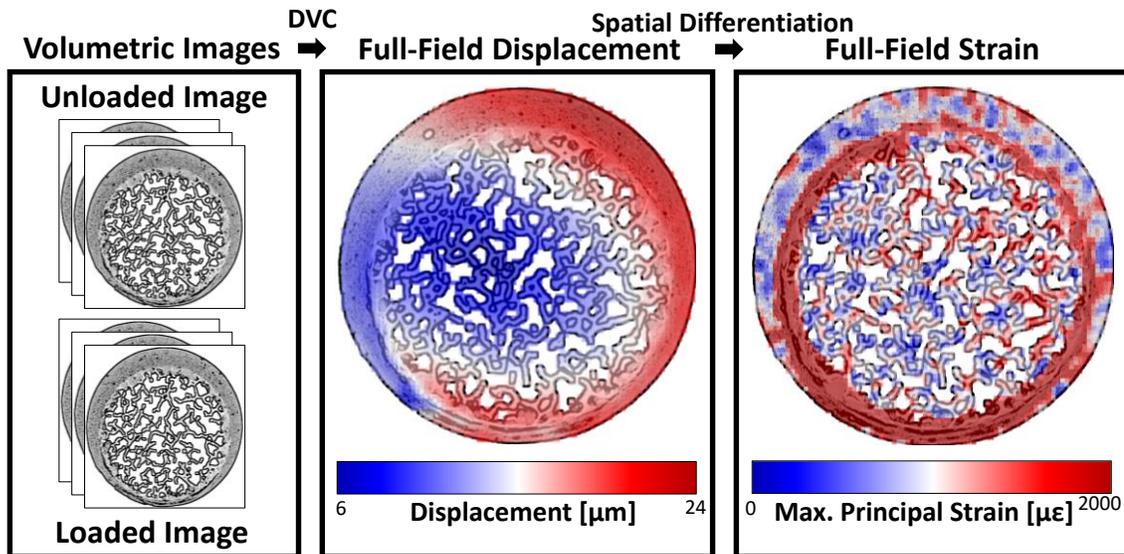
Figure 5: Overview of a local DVC approach with sample imagery.

1.9 Applications of DVC in Bone-Centric *in vitro* Models of Clinical Problems

The use of digital volume correlation combined with biomechanical testing to analyze bone strains is an active area of research. Many initial efforts were focused on quantifying the accuracy and precision of strain measurements derived from digital volume correlation in bone by developing relationships between common digital volume correlation and imaging parameters and measurement uncertainties.[44,51,52] New research seeks to leverage the practical application of digital volume correlation in investigations of gross clinical problems. In particular, the upper extremity, the glenohumeral joint, and orthopedic applications are being investigated using digital volume correlation. Tozzi et al. used digital volume correlation to assess microdamage to orthopedic bone-cement

interfaces under both monotonic and cyclic compression.[53] Boulaache et al. used micro-CT and DVC to investigate strain in the glenoid after anatomical total shoulder arthroplasty.[45] Zhou et al. analyzed glenoids before and after anatomic implant placement to determine the effect of glenoid implants on bone biomechanical response post-implantation. [54] These recent studies have used DVC to investigate the large-scale mechanics or small-scale mechanics of critical interfaces in the upper extremity, but a continuum between small-scale mechanics and large-scale understanding of the failure of some of these critical interfaces has not been well established. Both measurement uncertainty analyses within clinical problems and analyses attempting to probe the knowledge translation between small- and large-scale mechanics in the glenohumeral joint are investigated in this thesis.

1.10   Thesis Rationale

The synthesis of digital volume correlation and high-resolution x-ray computed tomography imagery enables the experimental investigation of many clinically relevant problems in the upper extremity. However, as this approach is still rapidly being developed in the wake of ever-increasing improvements to high-resolution volumetric imagery, it is important to understand its capabilities and limitations both qualitatively and quantitively in terms of important metrological parameters such as measurement accuracy and precision, and also in the context of real biomedical implant materials and problems.

Specifically, this thesis aims to investigate the viability of using digital volume correlation to elucidate the mechanical behaviour of interfaces that are thought to drive the clinical problems of aseptic glenoid loosening post-total shoulder arthroplasty and hemiarthroplasty glenoid erosion. After investigating the viability of the DVC approach in both of these problems, it will conclude with a study that aims to apply DVC to examine the mechanical behaviour of an interface that is thought to contribute to aseptic glenoid failure. The contribution of this thesis is twofold: firstly, it demonstrates a "start-to-finish" approach to DVC analyses in the upper extremity, transitioning from preliminary analysis of the metrological aspects of the DVC technique to DVC application; secondly, the application of the DVC technique contributes to the body of

knowledge surrounding failure initiation in the cement mantle of the glenoid, and corresponding aseptic glenoid loosening failure.

1.11   Objectives and Hypotheses

Objective 1-*(a)* To quantify the accuracy and precision of DVC-derived strain measurements in x-ray micro-CT imagery of unloaded scapulae containing glenoid implants and PMMA bone cement as a function of parameters of practical interest such as measurement resolution and volumetric image acquisition time *(b)* and to use those practical parameters to investigate the accuracy and precision of DVC-derived strain measurements of loaded scapulae containing glenoid implants and PMMA bone cement.

Hypothesis 1-*(a)* The measurement accuracy and precision of DVC-derived strain measurements in unloaded scapulae containing glenoid implants will allow for measurements that are physiologically relevant (i.e. substantially lower than commonly reported trabecular failure strains) at a measurement resolution no higher than 1mm. *(b)* This will also hold true in the examination of loaded scapulae, but the introduction of load will decrease the accuracy and precision of the corresponding measurements.

Objective (2)-*(a)* To quantify the accuracy and precision of DVC-derived strain measurements in x-ray micro-CT imagery of scapulae emulating a hemiarthroplasty procedure *(b)* and to quantify the relationship between distance to the implant and a statistically significant decrease in strain measurement accuracy and precision

Hypothesis 2-*(a)* Strain measurement accuracy and precision will be lower in hemiarthroplasty scapulae than those investigated previously the presence of image artifact inducing materials. The measurement accuracy and precision will still allow for physiologically relevant measurements, however *(b)* there will be statistically significant degradation of measurement accuracy and precision in measurements made in image slices containing the humeral head implant.

Objective 3-To investigate the effects of both a primarily tensile and primarily compressive displacement-control stepwise loading regime on maximum and minimum principal strains measured in an *in vitro* model of the peri-glenoid implant peripheral peg space.

Hypothesis 3-*(a)* There will be significant differences between maximum and minimum principal strains as a function of the location of measurement along the peg, *(b)* as a function of distance from the peg, *(c)* and as a function of the interaction between the effect of location of measurement along the peg and distance from the peg at all levels of displacement in both primarily tensile-based loads and primarily compressive-based loads.

1.12   Thesis Overview

Within this thesis, Chapter 2 investigates the accuracy and precision of a digital volume correlation approach in the load transfer under pegged and keeled glenoid implants fixed in cadaveric scapulae. Chapter 3 examines a similar problem to that posed in Chapter 2 in an investigation of the accuracy and precision of DVC strain measurements in CT images of scapulae confounded with artifacts caused by humeral head materials used in hemiarthroplasty. Chapter 4 transitions from a metrological examination of the DVC approach to a practical application of the DVC approach to investigate the load transfer in an *in vitro* model of the glenoid implant peripheral peg-bone cement-trabecular bone interface. Chapter 5 concludes with a summary of the findings of the previous chapters and suggests avenues of continuation for the research presented within.

1.13 References

1. Kim SH. Pathoanatomy of Glenohumeral Instability. *Normal and Pathological Anatomy of the Shoulder*. Published online 2015:115-122. doi:10.1007/978-3-662-45719-1_13

2. Provencher MT, Frank RF, Gross DJ, Golijanin P. Glenoid. *Normal and Pathological Anatomy of the Shoulder*. Published online 2015:35-45. doi:10.1007/978-3-662-45719-1_4

3. Malik SS, Malik SS. Biomechanics of the shoulder. *Orthopaedic Biomechanics Made Easy*. Published online 2015:126-135. doi:10.1017/CBO9781107360563.012

4. Chen J, Phadnis J. Glenohumeral and Ligaments. *Normal and Pathological Anatomy of the Shoulder*. Published online 2015:93-99. doi:10.1007/978-3-662-45719-1_10

5. Roach HI, Tilley S. The Pathogenesis of Osteoarthritis BT - Bone and Osteoarthritis. *Bone and Osteoarthritis*. Published online 2007:1-18. Accessed April 3, 2022. http://link.springer.com/10.1007/978-1-84628-701-5_1

6. Migliorini F, Vecchio G, Baroncini A, Pintore A, Oliva F, Maffulli N. Anatomic Total Shoulder Arthroplasty versus Hemiarthroplasty for Glenohumeral Osteoarthritis: A Systematic Review and Meta-Analysis. Published online 2021. doi:10.3390/app112110112

7. Buss DJ, Kröger R, McKee MD, Reznikov N. Hierarchical organization of bone in three dimensions: A twist of twists. *Journal of Structural Biology: X*. 2022;6:100057. doi:10.1016/J.YJSBX.2021.100057

8. Safadi FF, Barbe MF, Abdelmagid SM, et al. Bone structure, development and bone biology. *Bone Pathology*. Published online 2009:1-50. doi:10.1007/978-1-59745-347-9_1

9. Benjwal P, Balani K. Multi-Length Scale Hierarchy in Natural Materials. *Biosurfaces: A Materials Science and Engineering Perspective*. Published online January 16, 2015:146-169. doi:10.1002/9781118950623.CH5

10. Sabatini Massimo, Pastoureau Philippe, de Ceuninck F. Cartilage and osteoarthritis. Volume 2, Structure and in vivo analysis. Published online 2004:343.

11. Wyatt LA, Doherty M. Morphological aspects of pathology Chapter: Morphological aspects of pathology Oxford Textbook of Osteoarthritis and Crystal Arthropathy (3 ed.). Published online 2016. doi:10.1093/med/9780199668847.001.0001

12. Bigliani LU, Flatow EL. Shoulder arthroplasty. *Shoulder Arthroplasty*. Published online 2005:1-218. doi:10.1007/B138579

13. Klawitter JJ, Patton J, More R, Peter N, Podnos E, Ross M. In vitro comparison of wear characteristics of PyroCarbon and metal on bone: Shoulder hemiarthroplasty. *Shoulder & Elbow*. 2020;12(1 Suppl):11. doi:10.1177/1758573218796837

14. Wieczorek M, Rotonda C, Guillemin F, Rat AC. What Have We Learned About the Course of Clinical Outcomes After Total Knee or Hip Arthroplasty? *Arthritis Care and Research*. 2020;72(11):1519-1529. doi:10.1002/ACR.24045/ABSTRACT

15. Schwartz BE, Savin DD, Youderian AR, Mossad D, Goldberg BA. National trends and perioperative outcomes in primary and revision total shoulder arthroplasty: Trends in total shoulder arthroplasty. *International Orthopaedics*. 2015;39(2):271-276. doi:10.1007/S00264-014-2614-5/FIGURES/4

16. Raiss P, Bruckner T, Rickert M, Walch G. Longitudinal observational study of total shoulder replacements with cement fifteen to twenty-year follow-up. *Journal of Bone and Joint Surgery - Series A*. 2014;96(3):198-205. doi:10.2106/JBJS.M.00079

17. Bonnevialle N, Melis B, Neyton L, et al. Aseptic glenoid loosening or failure in total shoulder arthroplasty: revision with glenoid reimplantation. doi:10.1016/j.jse.2012.08.009

18. Sundfeldt M, Carlsson L v., Johansson CB, Thomsen P, Gretzer C. Aseptic loosening, not only a question of wear: A review of different theories. *Acta Orthopaedica*. 2006;77(2):177-197. doi:10.1080/17453670610045902

19. Papadonikolakis A, Neradilek MB, Matsen FA. Failure of the Glenoid Component in Anatomic Total Shoulder Arthroplasty. *The Journal of Bone and Joint Surgery-American Volume*. 2013;95(24):2205-2212. doi:10.2106/jbjs.l.00552

20. Parsons IM, Millett PJ, Warner JJP. Glenoid Wear after Shoulder Hemiarthroplasty. *Clinical Orthopaedics & Related Research*. 2004;421:120-125. doi:10.1097/01.BLO.0000119249.61696.F1

21. Barret H, Gauci MO, Langlais T, van der Meijden O, Tran L, Boileau P. Pyrocarbon interposition shoulder arthroplasty in young arthritic patients: a prospective observational study. *Journal of Shoulder and Elbow Surgery*. 2020;29(1):e1-e10. doi:10.1016/J.JSE.2019.05.044

22. Hannoun A, Ouenzerfi G, Brizuela L, et al. Pyrocarbon versus cobalt-chromium in the context of spherical interposition implants: An in vitro study on cultured Chondrocytes. *European Cells and Materials*. 2019;37:1-15. doi:10.22203/ECM.V037A01

23. Oftadeh R, Perez-Viloria M, Villa-Camacho JC, Vaziri A, Nazarian A. Biomechanics and Mechanobiology of Trabecular Bone: A Review. *Journal of Biomechanical Engineering*. 2015;137(1):0108021. doi:10.1115/1.4029176

24. Athanasiou KA, Wang X, Nyman JS, et al. Fundamental Biomechanics in Bone Tissue Engineering. *Synthesis Lectures on Tissue Engineering*. 2010;2(1):1-225. doi:10.2200/S00246ED1V01Y200912TIS004

25. Stauber M, Rapillard L, van Lenthe GH, Zysset P, Müller R. Importance of individual rods and plates in the assessment of bone quality and their contribution to bone stiffness. *Journal of Bone and Mineral Research*. 2006;21(4):586-595. doi:10.1359/JBMR.060102

26. Morgan EF, Keaveny TM. Dependence of yield strain of human trabecular bone on anatomic site. *Journal of Biomechanics*. 2001;34(5):569-577. doi:10.1016/S0021-9290(01)00011-2

27. Bayraktar HH, Morgan EF, Niebur GL, Morris GE, Wong EK, Keaveny TM. Comparison of the elastic and yield properties of human femoral trabecular and cortical

bone tissue. *Journal of Biomechanics*. 2004;37(1):27-35. doi:10.1016/S0021-9290(03)00257-4

28. Cooke SB, Terhune CE. Form, Function, and Geometric Morphometrics. *Anatomical Record*. 2015;298(1):5-28. doi:10.1002/AR.23065

29. Sylvester AD, Terhune CE. Trabecular mapping: Leveraging geometric morphometrics for analyses of trabecular structure. *American Journal of Physical Anthropology*. 2017;163(3):553-569. doi:10.1002/AJPA.23231

30. Dong P, Haupert S, Hesse B, et al. 3D osteocyte lacunar morphometric properties and distributions in human femoral cortical bone using synchrotron radiation micro-CT images. *Bone*. 2014;60:172-185. doi:10.1016/J.BONE.2013.12.008

31. Fajardo RJ, Müller R. Three-dimensional analysis of nonhuman primate trabecular architecture using micro-computed tomography. *American Journal of Physical Anthropology*. 2001;115(4):327-336. doi:10.1002/AJPA.1089

32. Klose-Jensen R, Tse JJ, Keller KK, et al. High-Resolution Peripheral Quantitative Computed Tomography for Bone Evaluation in Inflammatory Rheumatic Disease. *Frontiers in Medicine*. 2020;7. doi:10.3389/FMED.2020.00337

33. O'Neill F, Condon F, McGloughlin T, Lenehan B, Coffey C, Walsh M. Validity of synthetic bone as a substitute for osteoporotic cadaveric femoral heads in mechanical testing: A biomechanical study. *Bone & Joint Research*. 2012;1(4):50. doi:10.1302/2046-3758.14.2000044

34. Pekedis M, Yoruk MD, Binboga E, Yildiz H, Bilge O, Celik S. Characterization of the mechanical properties of human parietal bones preserved in modified larssen solution, formalin and as fresh frozen. *Surgical and Radiologic Anatomy*. 2021;43(12):1933-1943. doi:10.1007/S00276-021-02762-1/FIGURES/4

35. Cristofolini L, Viceconti M, Cappello A, Toni A. Mechanical validation of whole bone composite femur models. *Journal of Biomechanics*. 1996;29(4):525-535. doi:10.1016/0021-9290(95)00084-4

36. Knowles NK, Kusins J, Faieghi M, Ryan M, Dall'Ara E, Ferreira LM. Material Mapping of QCT-Derived Scapular Models: A Comparison with Micro-CT Loaded Specimens Using Digital Volume Correlation. *Annals of Biomedical Engineering*. 2019;47(11):2188-2198. doi:10.1007/s10439-019-02312-2

37. Lawless IM, Ding B, Cazzolato BS, Costi JJ. Adaptive velocity-based six degree of freedom load control for real-time unconstrained biomechanical testing. *Journal of Biomechanics*. 2014;47(12):3241-3247. doi:10.1016/J.JBIOMECH.2014.06.023

38. Grassi L, Isaksson H. Extracting accurate strain measurements in bone mechanics: A critical review of current methods. *Journal of the Mechanical Behavior of Biomedical Materials*. 2015;50:43-54. doi:10.1016/J.JMBBM.2015.06.006

39. Carriero A, Javaheri B, Bassir Kazeruni N, Pitsillides AA, Shefelbine SJ. Age and Sex Differences in Load-Induced Tibial Cortical Bone Surface Strain Maps. *JBMR Plus*. 2021;5(3). doi:10.1002/JBM4.10467

40. Roriz P, Carvalho L, Frazão O, Santos JL, Simões JA. From conventional sensors to fibre optic sensors for strain and force measurements in biomechanics applications: A review. *Journal of Biomechanics*. 2014;47(6):1251-1261. doi:10.1016/J.JBIOMECH.2014.01.054

41. Marter A, Burson-Thomas C, Dickinson A, et al. Measurement of Internal Implantation Strains in Analogue Bone Using DVC. *Materials*. 2020;13(18). doi:10.3390/MA13184050

42. Ghosh R, Gupta S, Dickinson A, Browne M. VERIFICATION OF THE DIGITAL IMAGE CORRELATION TECHNIQUE FOR BONE SURFACE STRAIN MEASUREMENTS. *Journal of Biomechanics*. 2012;45:S277. doi:10.1016/S0021-9290(12)70278-6

43. Bay BK, Smith TS, Fyhrie DP, Saad M. Digital volume correlation: Three-dimensional strain mapping using x-ray tomography. *Experimental Mechanics*. 1999;39(3):217-226. doi:10.1007/BF02323555

44.   Palanca M, Tozzi G, Cristofolini L, Viceconti M, Dall'Ara E. Three-Dimensional Local Measurements of Bone Strain and Displacement: Comparison of Three Digital Volume Correlation Approaches. *Journal of Biomechanical Engineering*. 2015;137(7). doi:10.1115/1.4030174

45.   Boulanaache Y, Becce F, Farron A, Pioletti DP, Terrier A. Glenoid bone strain after anatomical total shoulder arthroplasty: In vitro measurements with micro-CT and digital volume correlation. *Medical Engineering and Physics*. 2020;85:48-54. doi:10.1016/j.medengphy.2020.09.009

46.   Palanca M, Cristofolini L, Dall'Ara E, et al. Digital volume correlation can be used to estimate local strains in natural and augmented vertebrae: An organ-level study. *Journal of Biomechanics*. 2016;49(16):3882-3890. doi:10.1016/j.jbiomech.2016.10.018

47.   Rapagna S, Berahmani S, Wyers CE, et al. Quantification of human bone microarchitecture damage in press-fit femoral knee implantation using HR-pQCT and digital volume correlation. *Journal of the Mechanical Behavior of Biomedical Materials*. 2019;97:278-287. doi:10.1016/j.jmbbm.2019.04.054

48.   Hsieh J. Computed Tomography, Second Edition. *Computed Tomography, Second Edition*. Published online October 26, 2009. doi:10.1117/3.817303

49.   du Plessis A, Broeckhoven C, Guelpa A, le Roux SG. Laboratory x-ray micro-computed tomography: a user guideline for biological samples. *Gigascience*. 2017;6(6):1. doi:10.1093/GIGASCIENCE/GIX027

50.   van Dijk NP, Wu D, Persson C, Isaksson P. A global digital volume correlation algorithm based on higher-order finite elements: Implementation and evaluation. *International Journal of Solids and Structures*. 2019;168:211-227. doi:10.1016/J.IJSOLSTR.2019.03.024

51.   Liu L, Morgan EF. Accuracy and precision of digital volume correlation in quantifying displacements and strains in trabecular bone. *Journal of Biomechanics*. 2007;40:3516-3520. doi:10.1016/j.jbiomech.2007.04.019

52. Dall'Ara E, Peña-Fernández M, Palanca M, Giorgi M, Cristofolini L, Tozzi G. Precision of digital volume correlation approaches for strain analysis in bone imaged with micro-computed tomography at different dimensional levels. *Frontiers in Materials*. 2017;4:31. doi:10.3389/fmats.2017.00031

53. Tozzi G, Zhang QH, Tong J. Microdamage assessment of bone-cement interfaces under monotonic and cyclic compression. *Journal of Biomechanics*. 2014;47(14):3466-3474. doi:10.1016/J.JBIOMECH.2014.09.012

54. Zhou Y, Gong C, Lewis GS, Armstrong AD, Du J. 3D full-field biomechanical testing of a glenoid before and after implant placement. *Extreme Mech Lett*. 2020;35:100614. doi:10.1016/J.EML.2019.100614

2   Assessing Methodological Uncertainty of *in vitro* Digital Volume Correlation Bone Strain Measurements in Total Shoulder Arthroplasties[*]

OVERVIEW

Digital volume correlation (DVC) performed on micro-computed tomography (CT) imagery provides a measurement technique which can measure full-field deformations of loaded osseous tissues. This experimental approach is of interest in the investigation of the failure mechanisms of glenoid implants in total shoulder arthroplasties, as it allows for direct experimental measurement of strains at the bone-cement-implant interface. It is therefore important to understand the methodological limitations of the bone strain measurements made and the inherent uncertainty present in this approach. Micro-CT scans of two cadaveric scapulae from donors who had been treated with shoulder replacement in life were captured with differing numbers of CT projections under loaded and unloaded conditions. DVC strain measurements were quantified from the unloaded and loaded volumetric images with five distinct sub-volume sizes. The strain mean absolute error and standard deviation of error were quantified in the DVC strains as a function of projection count and sub-volume size, establishing relationships between measurement spatial resolution, image quality, and strain measurement error. Observations reveal that with careful selection of DVC spatial resolution and CT projection count, scan times can be halved with no impact on DVC strain accuracy. Thus, DVC can be a useful preclinical evaluation tool to quantify the internal strain within bone-implant constructs.

---

[*]A version of this work has been accepted for publication: Targosinski, J., Kusins, K., Martensson, N., Nelson, A., Knowles, N., Ferreira, L. "Assessing methodological uncertainty of in-vitro digital volume correlation bone strain measurements in total shoulder arthroplasties," Lecture Notes in Computational Vision and Biomechanics. (2022)

2.1 Introduction

In combination with micro-computed tomography (micro-CT) imaging, digital volume correlation (DVC) has the potential to enable full-field strain measurements within bone. [1–4] The DVC method offers the ability to assess internal bone strain, not possible with conventional surface measurement techniques such as strain gauges and digital image correlation (DIC), which are further limited to discrete locations (strain gauges) or sub-regions on the surface of the specimen (DIC).[5]

Glenoid implants, which serve as the replacement for the articular surface of the scapula in patients who undergo total shoulder arthroplasty procedures, are a class of implant which are of particular interest to the practical application of DVC-based strain measurement methods. The long-term outcomes of glenoid implants remain relatively poor compared to other joint arthroplasties, with symptomatic glenoid failure occurring at a mean annualized rate of 1.2% after primary surgery.[6] The most common failure mode of these implants is the loosening of the glenoid implant from its fixation within bone. It is currently believed that the cause of glenoid loosening failure is mechanical: the rocking-horse effect, where cyclic eccentric loading of the glenoid rim induces excessive mechanical stresses causing progressive damage to the cement mantle-bone interface.[7,8] However, the direct measurement of the mechanical behavior at this interface is difficult, and currently the only experimental measurement technique that can probe this interface directly involves the combination of high resolution volumetric imaging with DVC.[9,10] Finite element models have also investigated the behavior of the implant-bone-cement interface, but rely on bone density-material property relationships that can have a large impact on the predicted outcomes of these models.[11–15]

Strain measurements derived from DVC face issues with validation, as no other measurement tool can provide full-field strain measurements of the same caliber; thus, it is difficult to comparatively assess the accuracy and precision of DVC strains made against previously validated measurements acquired through other metrological

approaches. It is therefore of importance to assess the strain measurement error associated with methodologies that aim to employ DVC to quantify strain in the glenoid implant-cement-bone interface and in other arthroplasties. Various methods exist in the literature for assessing DVC measurement error. Some have used a zero-strain assumption approach in which they comparatively assess the strain between two unloaded volumetric images and use the disagreement between the DVC-measured strain and the idealized zero-strain condition as a measure of the methodological error.[3] Others have used digital affine transformations of volumetric images to impose a known virtual strain and then quantified the error as a function of the disagreement between the known virtual strain and the DVC-measured strain.[4] *In vitro* DVC strain measurement error in the glenoid implant-bone-cement interface has been recently analyzed, but the relationship between image acquisition time and DVC sub-volume size was not reported [16]. The goal of the current study was to quantify the experimental uncertainties associated with the use of DVC to measure full-field strains in underlying scapular bone following a shoulder arthroplasty procedure. Specifically, this study quantified (1) the influence of imaging acquisition time and (2) the global DVC sub-volume size on the accuracy and precision of the measured osseous strains in cadaveric shoulders under unloaded and loaded conditions.

2.2   Methods

Two independent variables were established representing factors of image quality and spatial resolution of the strain measurement: 1) CT projection slice count was varied to investigate the effect of image quality; and 2) the global DVC sub-volume size was varied to investigate the effect of varying strain measurement resolution. Improved CT image quality can alter the experimental uncertainty of associated DVC strain measurements by providing bone structural information unconfounded by imaging artifacts. Similarly, increasing the sub-volume size also improves the DVC strain uncertainty, but both changes can have a significant impact on the time it takes to complete any single analysis.[3] Therefore, it is of practical concern to quantify the error response of both parameters in order to optimize the time needed to complete a DVC measurement with an acceptable level of error.

2.2.1   Specimen Preparation and Experimental Protocol

Two cadaveric scapulae, from donors previously treated with total shoulder arthroplasty procedures (79-year old male and 83-year old male), were recovered and denuded of all soft tissue, in accordance with institutional ethics (HSREB#113023). One scapula contained a pegged glenoid implant and the other contained a keeled glenoid implant; two implant designs with significant clinical relevance due to their overwhelming prevalence. The medial borders of the scapulae were cut parallel to the glenoid cavity at a distance of 10 cm from the articular surface and subsequently potted using polymethyl methacrylate (PMMA) bone cement. A CT-compatible loading hexapod robot (Stewart platform) was used to apply external loads to the cadaveric specimens directly within a cone-beam micro-CT scanner (XTH 225ST, Nikon, Minato, Japan) [14]. The hexapod robot (Picard Industries, Albion, NY, USA) was augmented with carbon-fiber struts for radiolucency, and a vise clamp fixed within the robot was used to locate and clamp the specimen.

For both cadaveric scapulae, the experimental loading protocol was as follows: prior to loading the scapula, two sets of micro-CT images were captured in an unloaded state (33.5μm isotropic voxel size, 95kVp, 64 μa, 1000 ms exposure). A 10 N load was applied to stabilize the specimen and ensure no bulk relative motion between the two captured volumetric images for the unloaded state. This load was measured through a 6-axis load cell (mini 45, ATI Industrial Automation, Apex, NC, USA) instrumented within the hexapod. To investigate the influence of acquisition time and image quality on the experimental uncertainties, two sets of unloaded scans were acquired with a varied number of projections (3141, 1571, 785, 393, 196) corresponding to various scan acquisition times (52, 26, 13, 6 and 3 minutes, respectively). The scapula was then subjected to a 750 N compressive axial load, and after allowing for viscoelastic relaxation of the bone to a steady state, additional micro-CT images were captured of the loaded scapulae at the same projection slice counts and imaging parameters (Fig. 6).
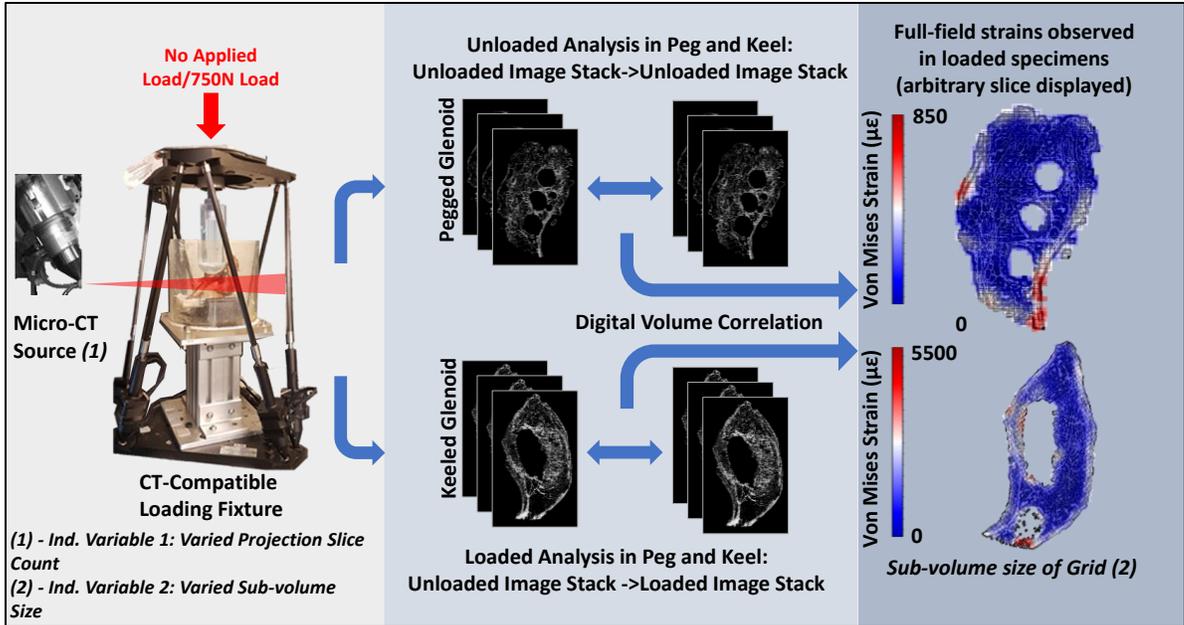
Figure 6. Simplified workflow of the unloaded and loaded DVC analyses performed. For the unloaded analysis, every combination of the two independent variables was investigated. For the loaded analysis, the spatial resolution of the DVC measurement was fixed based on the findings of the unloaded analysis at a value of 1072 μm (32 voxels).

2.2.2 Image Processing for DVC

Prior to the DVC analyses, the micro-CT images were post-processed using a consistent workflow to isolate the trabecular structure of the glenoid. The images were first cropped to a region of interest centered on the glenoid. The region of interest was chosen based on the 3141-projection volumetric images for both the pegged and keeled implants, and subsequently used for the remainder of the volumes. A specimen-specific thresholding operation was applied to each image with threshold limits decided subjectively by an experienced user based on the 3141-projection volumes, and afterwards applied to all subsequent CT projection-varied volumes. This was followed by a region growing operation (Mimics 20.0.0, Materialise, Leuven, Belgium) with a seed point selected within the trabecular structure isolated using the thresholding operation. The images were then converted to 8-bit grey scale, and manually registered to the unloaded images using an interactive program by aligning the borders of the cortical bone (MeVis Lab 3.4.1, MeVis Medical Solutions, Bremen, Germany) prior to running the DVC analyses.

A commercially available DVC implementation (DaVis 10.1.1, LaVision, Gottingen, Germany) was used to perform DVC at varied sub-volume sizes (8, 16, 32, 64, 128 voxels) on the two sets of unloaded images. An FFT pre-shift window size of 128, and a valid voxel requirement of 50% was used. A 0% sub-volume overlap was used for each sub-volume size. DaVis uses a hybrid DVC approach, which combines an initial FFT-DVC step to find large particle shifts and to create an initial predictor field, and subsequent direct DVC passes to find a solution for each shifted sub-volume. The local displacements, calculated by DVC, between the two images are then differentiated using a center finite difference (CFD) scheme to calculate strain.

2.2.3   Unloaded Uncertainty Analysis

An uncertainty analysis was performed in order to determine the accuracy and precision of the DVC strain measurements taken of the glenoid bone.[3,18] For each set of DVC measurements, a Matlab (The Mathworks, Natick, MA, USA) script extracted the strain tensors at each node, and two measures were defined to represent the accuracy and precision of the DVC approach employed. The mean absolute error (MAE) (Eq. 2) was defined as the mean of the absolute values of the strain tensor elements from each voxel, and the standard deviation of error (SDE) (Eq. 3) was defined as the standard deviation of the absolute values of the strain tensor elements from each voxel:[4]

$$Eq.\,2,\, MAE = \frac{\sum_{(i,j,k)} \left(\frac{\left(|\varepsilon_{xx}| + |\varepsilon_{yy}| + |\varepsilon_{zz}| + |\gamma_{xy}| + |\gamma_{xz}| + |\gamma_{yz}| \right)}{6} \right)_{i,j,k}}{N}$$

$$Eq.\,3,\, SDE = \sqrt{\frac{\sum_{i,j,k} \left| \frac{\left(|\varepsilon_{xx}| + |\varepsilon_{yy}| + |\varepsilon_{zz}| + |\gamma_{xy}| + |\gamma_{xz}| + |\gamma_{yz}| \right)_{i,j,k}}{6} - MAE \right|^2}{N}}$$

where $\varepsilon_{m,n}$ and $\gamma_{m,n}$ are the components of the strain tensor at the sub-volume located at position i, j, k, and N is the total number of sub-volumes in the DVC analysis. Power law fits were constructed for each set of MAE and SDE measurements of error by first linearizing the data and then fitting a first-order polynomial. Power law coefficients were

then extracted from the first-order polynomial coefficients. The linearization was performed to achieve a uniform regression response across the data set.

2.2.4   Loaded Uncertainty Analysis

Based on the accuracy (i.e., MAE) and precision (i.e., SDE) determined by the sensitivity analysis of the unloaded scans, a DVC sub-volume size of 1072 μm (32 voxels) was chosen as the best compromise between spatial resolution and the apparent strain measurement error. DVC bone strain measurements were taken from the loaded scans of the glenoids at each number of CT projections (3141, 1571, 785, 393, 196). For each set of DVC measurements, the difference in strain between the DVC measurement and the corresponding 3141-projection measurement was calculated for each DVC sub-volume. The mean difference in sub-volume strain and standard deviation of the strain differences between the sub-volumes served as analogous measures to the MAE and SDE used in the unloaded analysis. These were used as a measure of the overall methodological error and repeatability inherent in our DVC strain measurement process.

2.2.5   Bone Morphometric Parameters

BV/TV, Tb. Th., Tb. Sp. And Tb. N. were calculated from virtual volumes of interest selected from both scapulae. As much of the sub-glenoidal bone contained PMMA bone cement and the glenoid implants, the virtual volumes of interest contained the bone below the bottom of the implant cement and excluded the cortical shell. 1 cm of trabeculae in the medial-lateral direction were included in the volume of interest.

2.3   Results

Improving image quality by increasing the number of projections used to capture the volumetric images decreased the MAE and SDE. Likewise, decreasing the DVC measurement spatial resolution decreased the MAE and SDE for both the pegged and keeled glenoid implant designs.
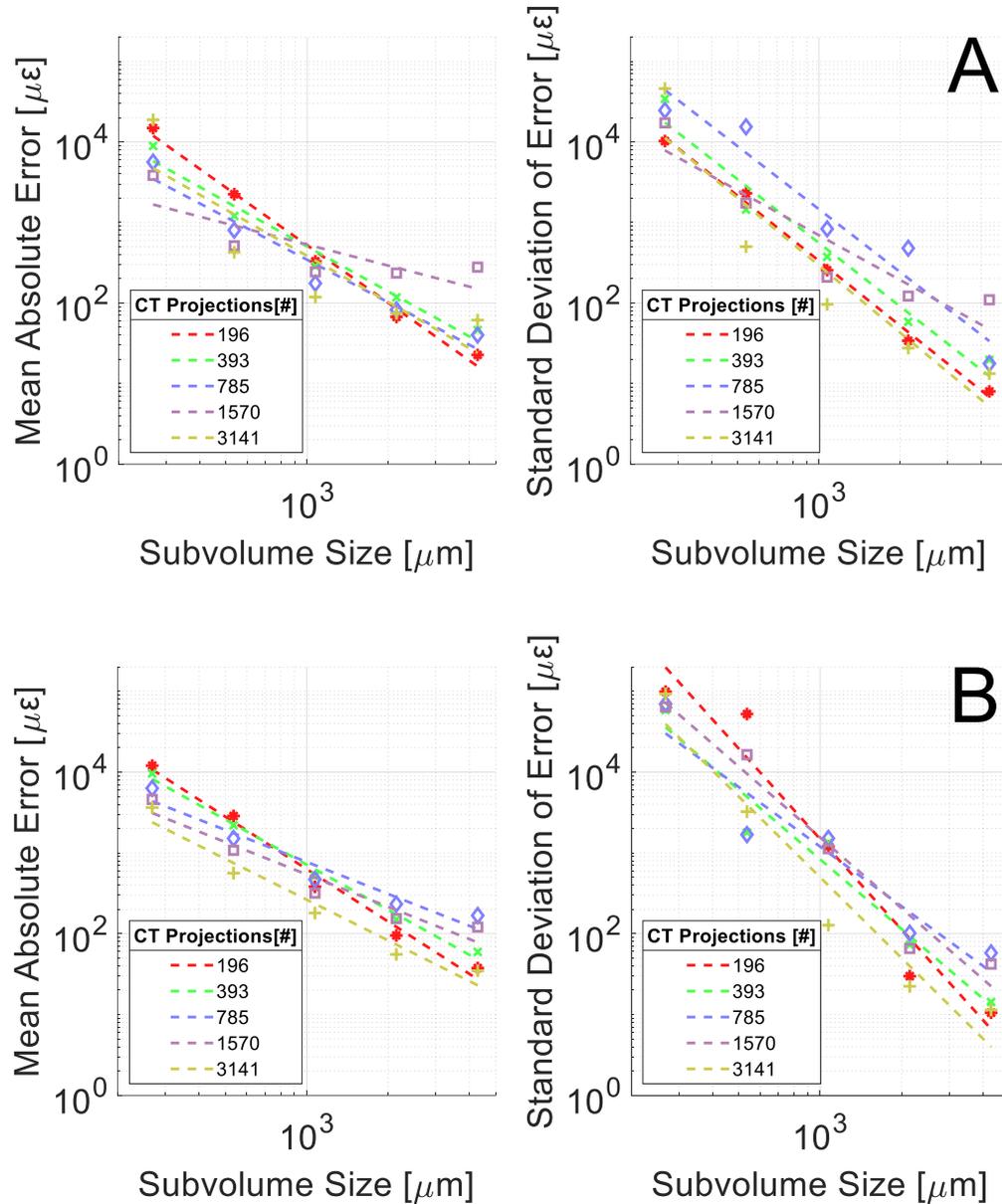
Figure 7: Mean absolute error (MAE) and standard deviation of error (SDE) in the unloaded scans of the keeled implant (A) and pegged implant (B) displayed with power law regressions corresponding to projection slice counts.

For a spatial resolution of 1072 µm (32 voxel sub-volume size), the accuracy and precision (MAE and SDE) of the strain measurements with the keeled implant ranged between 118-330 µε and 96-833 µε, respectively (Fig. 7). With the pegged implant, the

values were similar as determined through the unloaded analysis, with accuracy and precision ranging between 180-518 με and 128-1206 με, respectively.

At the selected strain measurement resolution of 32 voxels (1072 μm) in the loaded analysis, both the mean relative difference between the sub-volume strains, and the standard deviation of the relative difference, grew as a function of decreasing CT projection count for both implant designs (Fig. 8). For CT projection counts de-creasing from 3141 to 196, the corresponding mean relative differences ranged 588-6473 με for the keeled implant, and 583-2871 με for the pegged implant. Similarly, one standard deviation ranged 1508-7664 με and 675-3587 με for the keeled and pegged implants, respectively. A CT projection count of 1570 produced similar error to the 3141 projection measurements across both implants.
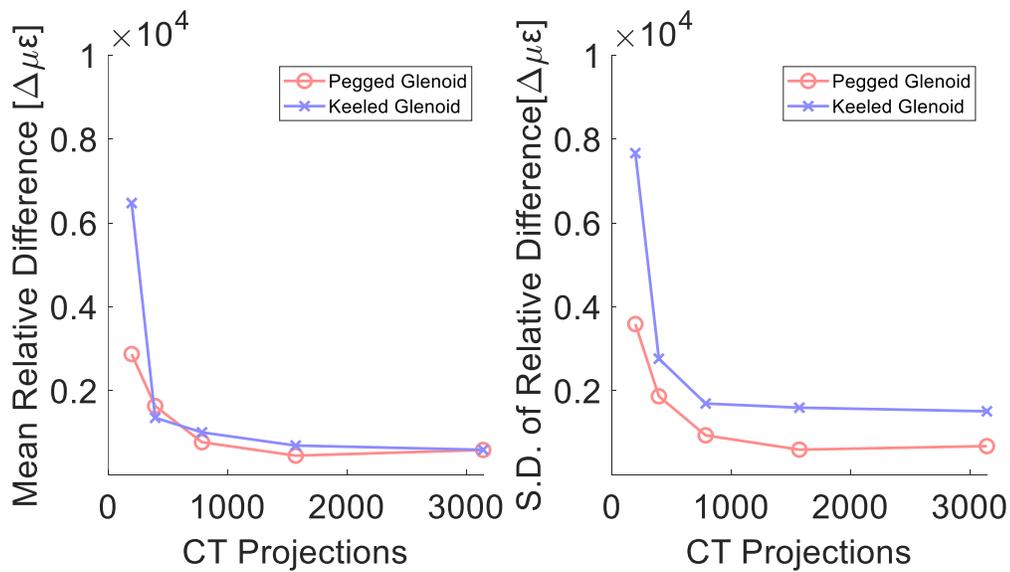
Figure 8: Performance of DVC as a function of CT projections and implant fixation type. Mean relative and 1 standard deviation of the strain difference are shown for projection counts of 3141, 1570, 785, 393, and 196 as a fraction of the 3141 reference DVC performance metrics. All measurements were taken at a sub-volume size of 32 voxels (1072 μm).

Locations of high strains were in the cortical shell throughout the glenoid, though the strains were particularly high underneath the glenoid implant pegs and keel in areas

where the glenoid narrowed as it joined with the subscapular fossa. The trabeculae in these areas also experienced high strains, as did those adjacent to the cement mantle of the implants (Fig. 9). The capability to make these observations decreased as the number of projections decreased as the strain field was overcome by apparent error.
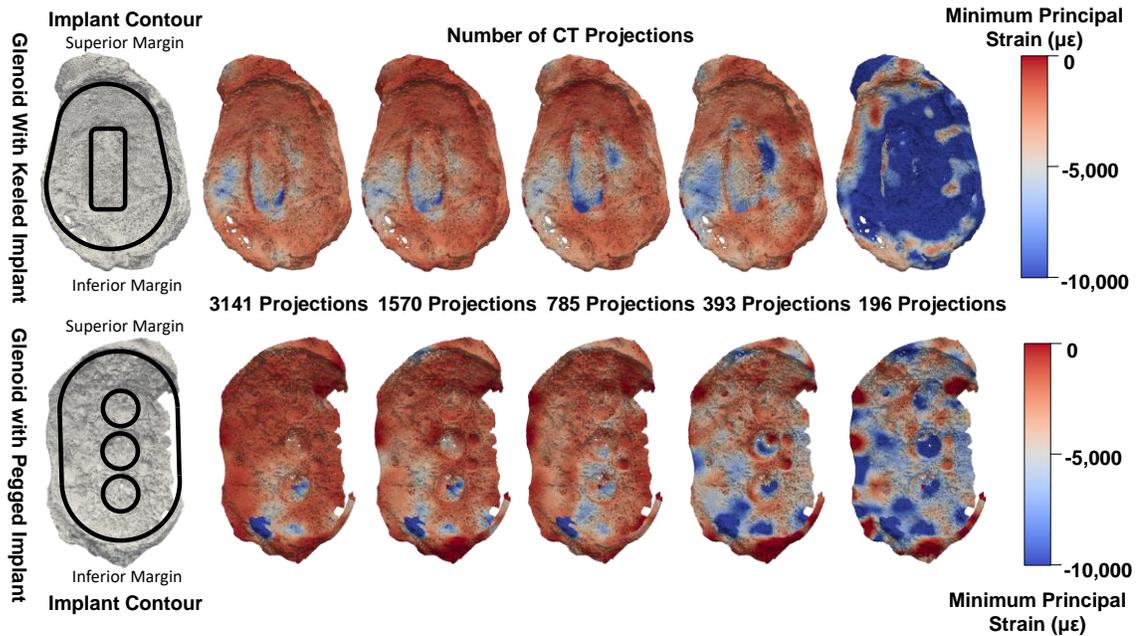
Figure 9: Minimum principal strains measured through DVC in the glenoid under both implants at 750N from DVC analyses performed on 3141, 1570, 785, 393 and 196 CT projection images. As the number of CT projections falls, the strain measurements rise erroneously.

Table 1: Morphometric parameters describing trabecular structure in both keeled and pegged glenoids.

Implant Type	BV/TV [%]	Tb. Th. [mm]	Tb. Sp. [mm]	Tb. N. [1/mm]
Peg	27.9	0.192	0.642	1.456
Keel	44.1	0.337	0.535	1.309

2.4   Discussion

This study provides guidance to optimize DVC bone strain measurement error while minimizing scan time using commercially available local DVC software. This investigation quantified the methodological uncertainties associated with measuring full-field strains within glenoid implant fixation in cadaveric scapular specimens from donors who had been treated with total shoulder arthroplasty in life. Based on the accuracy and precision determined by a sensitivity analysis in unloaded scans with a zero-strain assumption, a DVC sub-volume size of 1072 μm (32 voxels) was chosen as the best compromise between spatial resolution and the apparent strain measurement error. Comparatively, the mean relative difference and the standard deviation of the relative difference, which can be thought of as the error associated with performing the whole DVC-based methodology on loaded specimens, was approximately a half order of magnitude higher across each measured level. This could be due to methodological errors such as not allowing for enough relaxation time to reach a steady state in the osseous tissue. Other studies have reported similar magnitudes of MAE and SDE for *in vitro* DVC within the glenoid peri-implant space.[16]

Image quality as affected by the number of CT projections, had a strong effect on the accuracy and precision of loaded strain measurements, reaching a plateau beyond 785 CT projections (Fig. 8). From our results, there was no benefit beyond 1570 CT projections with the scanner used, which translates to a decrease in acquisition time of 50% relative to the 3141 CT projection scans. This can compound to substantial savings in stepwise loading study protocols that often require several loading levels multiplied by the number of implants being compared, along with any other factors being tested. A limitation of this study is that, in the loaded condition, the two 3141-projection count scans (one for reference) showed a mean relative difference of approximately 600 με (Fig. 8). Ideally, this would have been near zero. This encapsulates the repeatability of the entire DVC+micro-CT strain measurement methodology used, which would be influenced by factors such as relaxation of the cadaveric tissue, thermal expansion of the cadaveric tissue as it reached an equilibrium temperature within the micro-CT and relaxation of the loading fixture over time. Notably, relaxation in the fixture and relaxation of the

cadaveric tissue would likely be more impactful at higher loads, which was consistent with the observation that the relative error between loaded DVC analyses was higher than the absolute errors observed in the unloaded DVC analyses.

A compressive yield strain of ~7,000-40,000 $\mu\varepsilon$ at the apparent level has been reported for trabecular bone.[19–22] It is important to contextualize that in the loaded measurements of this study, the mean relative error did not exceed 9.8% of the lower bound of this value using the 1570 CT projection imagery. Moreover, the standard deviation of the relative error in the 1570 CT projection measurements was 22.7% of the lower bound of this value. This means that the DVC strain measurements captured through the methodology employed in this paper are physiologically relevant in the trabecular network of the glenoid. It has been observed that local strains in individual trabeculae can be substantially higher than those observed at the apparent level, which may mean the threshold for the error of DVC measurements at lower sub-volume sizes could also be significantly higher.[23] It should also be noted that mechanical properties of trabecular bone are thought to be sensitive to anatomical site, and DVC strain measurement error considerations should be made with respect to any specific application.[19] Nonetheless, these error metrics indicate DVC strain measurements at the bone-cement-implant interface can be reliable if care is taken to select appropriate spatial resolutions for the measurements and due consideration is given to imaging quality.

2.5   Conclusion

The combined use of micro-CT imaging and DVC strain measurements has the potential to provide clinically relevant bone strain measurements at the bone-cement-implant interface of glenoid implants. Careful selection of CT projection count and DVC spatial resolution can halve the time of CT acquisition, with no negative impact on DVC strain measurements. This can ameliorate the time constraints of future studies with stepwise load protocols. This improvement will facilitate the use of DVC to improve implant designs, and in turn the long-term outcomes of shoulder arthroplasty procedures.

2.6 References

1. Liu L, Morgan EF. Accuracy and precision of digital volume correlation in quantifying displacements and strains in trabecular bone. *Journal of Biomechanics*. 2007;40(15):3516-3520. doi:10.1016/j.jbiomech.2007.04.019

2. Palanca M, Tozzi G, Cristofolini L, Viceconti M, Dall'Ara E. Three-Dimensional Local Measurements of Bone Strain and Displacement: Comparison of Three Digital Volume Correlation Approaches. *Journal of Biomechanical Engineering*. 2015;137(7). doi:10.1115/1.4030174

3. Dall'Ara E, Peña-Fernández M, Palanca M, Giorgi M, Cristofolini L, Tozzi G. Precision of digital volume correlation approaches for strain analysis in bone imaged with micro-computed tomography at different dimensional levels. *Frontiers in Materials*. 2017;4:31. doi:10.3389/fmats.2017.00031

4. Comini F, Palanca M, Cristofolini L, Dall'Ara E. Uncertainties of synchrotron microCT-based digital volume correlation bone strain measurements under simulated deformation. *Journal of Biomechanics*. 2019;86:232-237. doi:10.1016/j.jbiomech.2019.01.041

5. Grassi L, Isaksson H. Extracting accurate strain measurements in bone mechanics: A critical review of current methods. *Journal of the Mechanical Behavior of Biomedical Materials*. 2015;50:43-54. doi:10.1016/j.jmbbm.2015.06.006

6. Papadonikolakis A, Neradilek MB, Matsen FA. Failure of the glenoid component in anatomic total shoulder arthroplasty :A systematic review of the english-language literature between 2006 and 2012. *Journal of Bone and Joint Surgery - Series A*. 2013;95(24):2205-2212. doi:10.2106/JBJS.L.00552

7. Gregory T, Hansen U, Taillieu F, et al. Glenoid loosening after total shoulder arthroplasty: An in vitro CT-scan study. *Journal of Orthopaedic Research*. 2009;27(12):1589-1595. doi:10.1002/jor.20912

8.   Jackins SE, Barrett WP, Matsen FA. Glenoid loosening in total shoulder arthroplasty: Association with rotator cuff deficiency. *Journal of Arthroplasty*. 1988;3(1):39-46. doi:10.1016/S0883-5403(88)80051-2

9.   Zhou Y, Gong C, Lewis GS, Armstrong AD, Du J. 3D full-field biomechanical testing of a glenoid before and after implant placement. *Extreme Mechanics Letters*. 2020;35:100614. doi:10.1016/j.eml.2019.100614

10.   Sukjamsri C, Geraldes DM, Gregory T, et al. Digital volume correlation and micro-CT: An in-vitro technique for measuring full-field interface micromotion around polyethylene implants. *Journal of Biomechanics*. 2015;48(12):3447-3454. doi:10.1016/j.jbiomech.2015.05.024

11.   Cristofolini L, Schileo E, Juszczyk M, Taddei F, Martelli S, Viceconti M. Mechanical testing of bones: The positive synergy of finite-element models and in vitro experiments. *Philosophical Transactions of the Royal Society A: Mathematical, Physical and Engineering Sciences*. 2010;368(1920):2725-2763. doi:10.1098/rsta.2010.0046

12.   Knowles NK, Kusins J, Faieghi M, Ryan M, Dall'Ara E, Ferreira LM. Material Mapping of QCT-Derived Scapular Models: A Comparison with Micro-CT Loaded Specimens Using Digital Volume Correlation. *Annals of Biomedical Engineering*. 2019;47(11):2188-2198. doi:10.1007/s10439-019-02312-2

13.   Kluess D, Soodmand E, Lorenz A, et al. A round-robin finite element analysis of human femur mechanics between seven participating laboratories with experimental validation. *Computer Methods in Biomechanics and Biomedical Engineering*. 2019;22(12):1020-1031. doi:10.1080/10255842.2019.1615481

14.   Kusins J, Knowles N, Ryan M, Dall'Ara E, Ferreira L. Performance of QCT-Derived scapula finite element models in predicting local displacements using digital volume correlation. *Journal of the Mechanical Behavior of Biomedical Materials*. 2019;97:339-345. doi:10.1016/j.jmbbm.2019.05.021

15. Knowles NK, Langohr GDG, Faieghi M, Nelson AJ, Ferreira LM. A comparison of density–modulus relationships used in finite element modeling of the shoulder. *Medical Engineering and Physics*. 2019;66:40-46. doi:10.1016/j.medengphy.2019.02.005

16. Boulanaache Y, Becce F, Farron A, Pioletti DP, Terrier A. Glenoid bone strain after anatomical total shoulder arthroplasty: In vitro measurements with micro-CT and digital volume correlation. *Medical Engineering and Physics*. 2020;85:48-54. doi:10.1016/j.medengphy.2020.09.009

17. ASTM. Astm F2028-17. 2002;(January):1-15. doi:10.1520/F2028-17.Copyright

18. Liu L, Morgan EF. Accuracy and precision of digital volume correlation in quantifying displacements and strains in trabecular bone. *Journal of Biomechanics*. 2007;40:3516-3520. doi:10.1016/j.jbiomech.2007.04.019

19. Morgan EF, Keaveny TM. Dependence of yield strain of human trabecular bone on anatomic site. *Journal of Biomechanics*. 2001;34(5):569-577. doi:10.1016/S0021-9290(01)00011-2

20. Odgaard A, Hvid I, Linde F. Compressive axial strain distributions in cancellous bone specimens. *Journal of Biomechanics*. 1989;22(8-9):829-835. doi:10.1016/0021-9290(89)90066-3

21. Bayraktar HH, Morgan EF, Niebur GL, Morris GE, Wong EK, Keaveny TM. Comparison of the elastic and yield properties of human femoral trabecular and cortical bone tissue. *Journal of Biomechanics*. 2004;37(1):27-35. doi:10.1016/S0021-9290(03)00257-4

22. Nagaraja S, Couse TL, Guldberg RE. Trabecular bone microdamage and microstructural stresses under uniaxial compression. *Journal of Biomechanics*. 2005;38(4):707-716. doi:10.1016/J.JBIOMECH.2004.05.013

23. Turunen MJ, Le Cann S, Tudisco E, et al. Sub-trabecular strain evolution in human trabecular bone. *Scientific Reports 2020 10:1*. 2020;10(1):1-14. doi:10.1038/s41598-020-69850-x

3 Effect of Metal and Ceramic Artifacts on Digital Volume Correlation Strain Measurements in Shoulder Hemiarthroplasties

OVERVIEW

Glenoid erosion following hemiarthroplasty remains a major concern in young and active patients. The mechanism which drives glenoid erosion is thought to be connected to the material properties of the humeral head implant and the resulting stress distribution in the glenoid through a complex biomechanical process. A combination of micro-CT imagery and digital volume correlation can measure the full-field strains in the glenoid under arbitrary loading conditions *in vitro*, however, common materials used in humeral head implants can cause significant artifacts in micro-CT imagery. It is therefore critical to investigate the effect of artifact-causing humeral head materials on DVC-based full-field strain measurements in the glenoid. In this study, micro-CT images of a cadaveric scapula were obtained with and without the presence of two artifact-inducing humeral head implants. CoCrMo and alumina-toughened zirconia humeral heads were placed on the articular surface of the glenoid implant, and a zero-strain DVC uncertainty analysis was performed in order to quantify the measurement error and the region to which the error was localized in the glenoid. The images of the scapula affected by the humeral head artifacts were also compared to a reference image, and Dice similarity coefficients were calculated for each image slice. It was found that at a mean distance of 1.26mm and 0.86mm from the CoCrMo humeral head and alumina-toughened zirconia humeral head, respectively, the DVC results are significantly affected, and are likely not reliable. However, elsewhere in the glenoid, the measurement error levels were acceptable with the (MAE, SDE) being (222.3, 806.0) $\mu\varepsilon$ and (262.3, 113.1) $\mu\varepsilon$ for the CoCrMo humeral head and alumina-toughened zirconia humeral head, respectively, at a sub-volume size of 2.1mm. This constitutes an acceptable level of error, and future work into the relationship between hemiarthroplasty humeral head material properties and DVC derived stress distributions in the glenoid can be investigated.

3.1 Introduction

Recent advances in the quality of volumetric radiological imaging coupled with digital volume correlation (DVC) has allowed for the ability to experimentally measure full-field osseous strains throughout cadaveric shoulder specimens. Previously, this technique was applied to visualize the load transfer between a pegged and keeled ultra-high molecular weight polyethylene glenoid implant, the surrounding cement mantle, and the scapular bone to identify areas of high peri-implant bone strain and to assess the methodological uncertainties associated with these strain measurements. However, many shoulder implant systems currently on the market incorporate materials such as cobalt-chrome-molybdenum alloys and alumina/zirconia-based ceramics which have moderate to poor radiolucent properties, and consequently may cause serious image artifacts in the surrounding tissues.[1–3]

Metal and ceramic-caused artifacts produced in CT imagery can be formed by one of two phenomena: beam hardening or photon starvation. Beam hardening occurs when low-energy photons are attenuated to a greater degree than high energy photons—this disparity in attenuation becomes more dominant as the density of the material increases. Photon starvation occurs when insufficient quantities of photons transmit through a high-density material to reach the detector and "starve" the CT reconstruction algorithm of the relevant attenuation information along the paths that the photon would typically transit.[1,3,4] Due to the nature of tomographic reconstruction, these artifacts are necessarily unconfined to the materials causing the artifact and present in all imaged materials that exist along the path(s) from source to detector, though they are more pronounced in locations within and immediately adjacent to the artifact-inducing material. Both cobalt-chrome-molybdenum alloys and alumina/zirconia-based ceramics are high-density materials which have been shown to cause both of these classes of artifact-inducing phenomena in radiological imagery of protheses.[5]

Shoulder implants create interfaces directly between the implant materials and the tissues that bound them. In the case of shoulder hemiarthroplasty, the head of the humerus is resected and replaced with an implant that articulates directly on the glenoid cavity of the scapula. Current concerns with the long term outcomes of the hemiarthroplasty procedure

surround the erosion of the glenoid cavity due to the direct articulation of the humeral head replacement on the chondral tissue.[6–8] Since the elasticity of natural bone is much higher than that of the materials that typically replace the humeral head (i.e., metal and ceramic implants), it has been speculated that this difference in elasticity contributes to an accelerated rate of glenoid cavity erosion, and a difference in the type of cartilaginous tissue regrowth on the articular surface post-operatively.[9,10] To investigate how strain develops in the glenoid as a function of different implant materials and their respective material properties, DVC could be employed to measure the osseous strain distributions corresponding to different humeral head implant designs and materials. However, as digital volume correlation algorithms depend strongly on the bone tissue structural information captured in volumetric imagery, any artifacts in the presence of these implant systems that affect the image quality may have deleterious effects on the DVC strain measurement accuracy and precision. This study examines two implant systems, one utilizing a CoCrMo implant humeral head and one using an alumina-toughened zirconia ceramic implant humeral head, and quantifies the change in apparent bone structure and the DVC strain measurement uncertainties that present themselves in the presence of these artifact-inducing materials.

3.2   Methods

3.2.1   Cadaveric Specimen Preparation

One cadaveric shoulder was denuded of all soft-tissue and the medial borders of the scapula were cut parallel to the glenoid cavity at a distance of ~10 cm from the articular surface. The scapula was then potted in its fixation using poly-methyl methacrylate bone cement. For each implant system, the loading system was altered to accommodate the different humeral heads: for the CoCrMo humeral head (Affinis, Mathys, Bettlach, Switzerland), a machined acrylic cylinder was fitted with the humeral head implant. For the ceramic humeral head (Affinis Short, Mathys, Bettlach, Switzerland), a cadaveric humerus was cut approximately 15 cm from the proximal end, and the humeral head was resected. A press-fit stem was inserted into the humerus, and the cut humerus was potted in a threaded PVC tube using poly-methyl methacrylate bone cement.

3.2.2   Micro-CT Image Acquisition

The potted scapula was placed within a cone-beam micro-CT scanner (XTH 225ST, Nikon, Minato, Japan) and a volumetric image was captured without the presence of any metal or ceramic materials to be used as a reference image for the trabecular and cortical structure of the scapula. The scapula was then placed within a radiolucent 6-DOF hexapod robot (Picard Industries, Albion, NY, USA) to which the humeral head loading systems were fixed. The scapula was then subjected to a 10N alignment load to ensure no rigid body motion during the imaging period. Two volumes were captured of each humeral head interfacing with the scapula using the micro-CT scanner (33.5µm slice thickness, 150 kVp, 80 µa, 1000 ms exposure, 3141 CT projections).
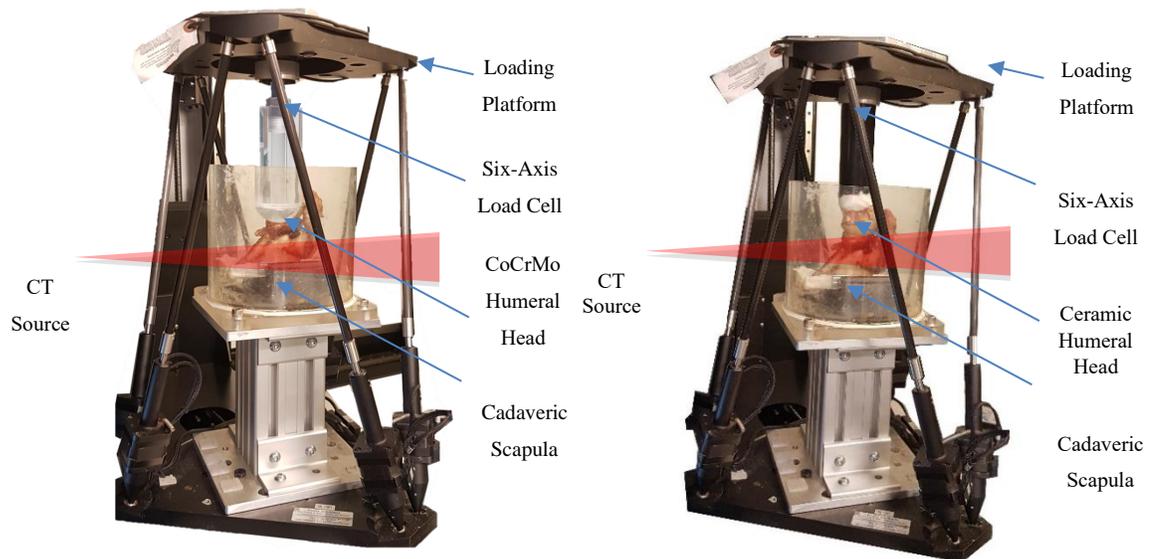
Figure 10: Loading fixtures emplaced within the radiolucent hexapod for both the ceramic and metallic humeral head implant.

3.2.3   Volumetric Image Post Processing

The resultant volumes were then segmented to isolate the scapular structure using Mimics software: 3D models of the humeral head implants were used to subtractively remove their presence from the image volume, and a combination of thresholding and region growing operations were used to subsequently isolate the scapula. Stereolithography 3D models of the scapula were constructed from the reference image. The volumetric

images were also converted from 16-bit grayscale to 8-bit grayscale for the digital volume correlation analysis.

3.2.4   Dice Coefficient Calculation

Using the isolated scapulae from each volumetric image, the Dice coefficient between the images containing the metal artifact and the reference scapula image was calculated in order to determine the effect of metal and ceramic artifact on the imaged structure of the scapular bone. The reference scapula was first globally registered to the scapula in the images containing the artifact, and the registered image was reconstructed using bicubic interpolation. The images were then converted to binary masks, and a common region of interest encompassing the glenoid ~2.5 cm (or 700 slices) from the articular surface was selected. The Dice coefficient (Eq. 4) is a measure of spatial overlap:

$$Eq.\,4, DSC = \frac{2|A \cap B|}{|A| + |B|}$$

Where A is the set of points corresponding to the scapula in the reference image, and B is the set of points corresponding to the scapula isolated from the images confounded by metal or ceramic artifacts and the square brackets denote the cardinality of a set. The value of the Dice coefficient as a function of distance from the artifact-inducing material was used as a measure of the degree to which the structural information of the bone was altered as a result of the material induced-artifacts.

3.2.5   Unloaded Digital Volume Correlation Analysis

In order to determine the accuracy and precision of the DVC strain measurements in the context of metal and ceramic artifact, an uncertainty analysis was performed with respect to the DVC sub-volume size. All DVC analyses were performed using a commercially available DVC package (DaVis 10.1.1, LaVision, Gottingen, Germany). DVC analyses were performed at sub-volume sizes of (8, 16, 32, 64, 128) voxels between the pairs of unloaded volumetric images of the scapula with the humeral head implants in the field of view. Strain tensors were extracted for each sub-volume in the analyses, and the mean

average error (MAE, Eq. 2) and standard deviation of error (SDE, Eq. 3) were calculated for each analysis, as defined in Chapter 2.

Power law fits were established for each set of MAE and SDE measurements through logarithmic linearization of the data and then fitting a first-degree polynomial to the augmented data set. This was done to ensure a uniform regression response across the entire range of error values. Correlation values for each node were also extracted and mapped onto models of the glenoid structure to analyze a potential location-correlation relationship. The correlation value (Eq. 1) in DaVis-DVC is:

$$C_{norm}(dx, dy, dz) = \sum_{(i,j,k)} \frac{(A_{i,j,k} - \langle A \rangle)(B_{i+dx,j+dy,k+dz} - \langle B_{dx,dy,dz} \rangle)}{\sqrt{|A'|^2} \sqrt{|B'_{dx,dy,dz}|^2}}$$

Where $A_{i,j,k}$ is the gray value intensity at the voxel position i, j, k in volume A and $B_{i+dx,j+dy,k+dz}$ is the gray value intensity in volume B at the position shifted by dx, dy, dz.

Sub-volume layer correlation values were also analyzed as a function of distance from the articular surface (i.e., the location of the artifact-inducing material) for every sub-volume size. A one-way ANOVA was used as an omnibus test to determine if there was a significant difference between correlation values as grouped by their distance from the articular surface, and a post-hoc Tukey HSD test was conducted to determine at what distance the correlation values corresponding to that layer group became significantly different from other sub-volume layers.

3.2.6   Bone Morphometric Parameters

Bone morphometric parameters corresponding to the same region of interest in the scapula were isolated from all three sets of images: the reference image of the scapula, the image containing the CoCr humeral head, and the image containing the ceramic humeral head. The scapulae were first registered to one another using a sum of square differences algorithm, and then a virtual volume of interest was isolated from each. These numbers were reported to allow for a qualitative comparison of the segmentation process.
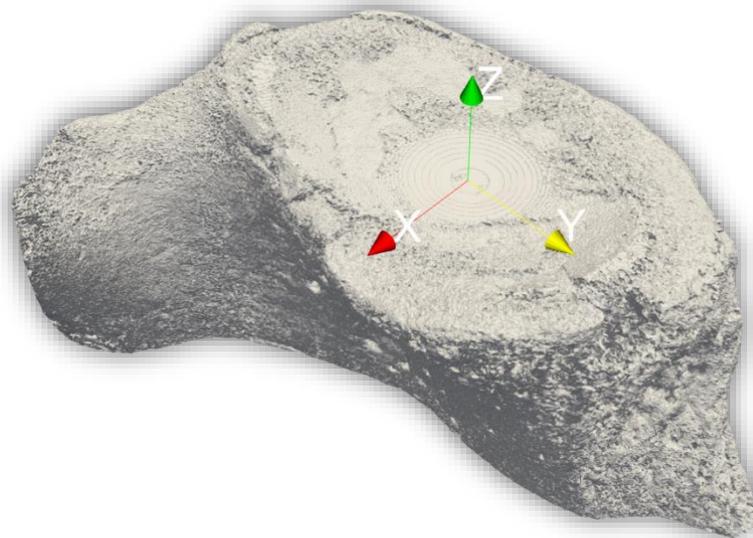
Figure 11: Coordinate system used in the context of the glenoid region of interest. The z-axis origin is located at the contact point of humeral head, with the positive direction oriented away from the articular surface. All distances noted as from the humeral head are with respect to this coordinate system.

3.3   Results

Fig. 12 shows the Dice similarity coefficient comparison between the reference scapula image and the images of the scapula containing the humeral heads showed a minimum Dice coefficient of 0.605 and a maximum value of 0.847 in the glenoid region below the ceramic humeral head. In the glenoid region below the CoCrMo humeral head, the minimum Dice coefficient was 0.658 and the maximum value was 0.817. As the region of interest became progressively smaller in the glenoid rim and the humeral head material artifact became more prominent in the slices containing the humeral head the Dice coefficient rapidly dropped to zero as speckle noise overlapped with progressively less of the segmented bone present in the reference image.

Table 2: Morphometric parameters describing trabecular structure isolated from a virtual volume of interest in the reference image of the scapula, the image containing the ceramic humeral head, and the image containing the CoCr humeral head.

Image	BV/TV [%]	Tb. Th. [mm]	Th. Sp. [mm]	Tb. N. [1/mm]
Reference	22.7	0.174	.610	1.301
Ceramic Humeral Head	17.6	0.195	.868	0.899
CoCr Humeral Head	25.4	0.261	0.805	0.967
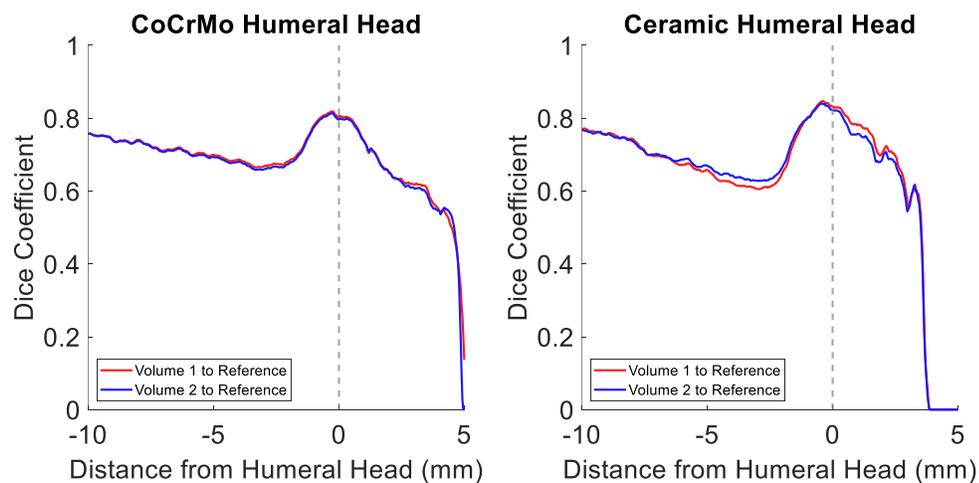
Figure 12: Dice coefficients of each segmented slice compared to the reference image of the scapula without artifacts. Coefficients decline initially then abruptly rise approximately 2.5mm from the humeral head implant (marked by dashed line). After this rise, the coefficients decline again in the CT slices containing the humeral head implants. Coordinate system is as described in Fig. 11.

Fig. 4 illustrates how the artifacts induced by the two humeral heads influence the DVC correlation values in the glenoid rim. As the sub-volume size shrinks (a measure of the

spatial resolution of the measurement), the correlation values in the glenoid rim correspondingly grow smaller. Though there are natural fluctuations in the correlation values throughout the glenoid, the distance vs. mean correlation value relationship in Fig. 14 display a clear trend of mean correlation value decrease beginning ~1mm away from the humeral head implant. It should be noted that as the sub-volumes grow larger, the regions which the sub-volume encompass grow as well—therefore the sub-volumes closest to the humeral head at the largest sub-volume size of 128 voxels contain regions of the volumetric images from both sides of the humeral head implant.

The mean distance below the implants at which the mean correlation values becomes significantly different (Table 3) from the adjacent sub-volume layers ($p<0.001$) was 0.862mm for the ceramic humeral head and 1.259mm for the CoCrMo humeral head. At the smallest sub-volume size (best measurement spatial resolution) of 8 voxels (0.268mm), the values were largely different: 1.398mm for the ceramic humeral head and 0.293mm for the CoCrMo humeral head.
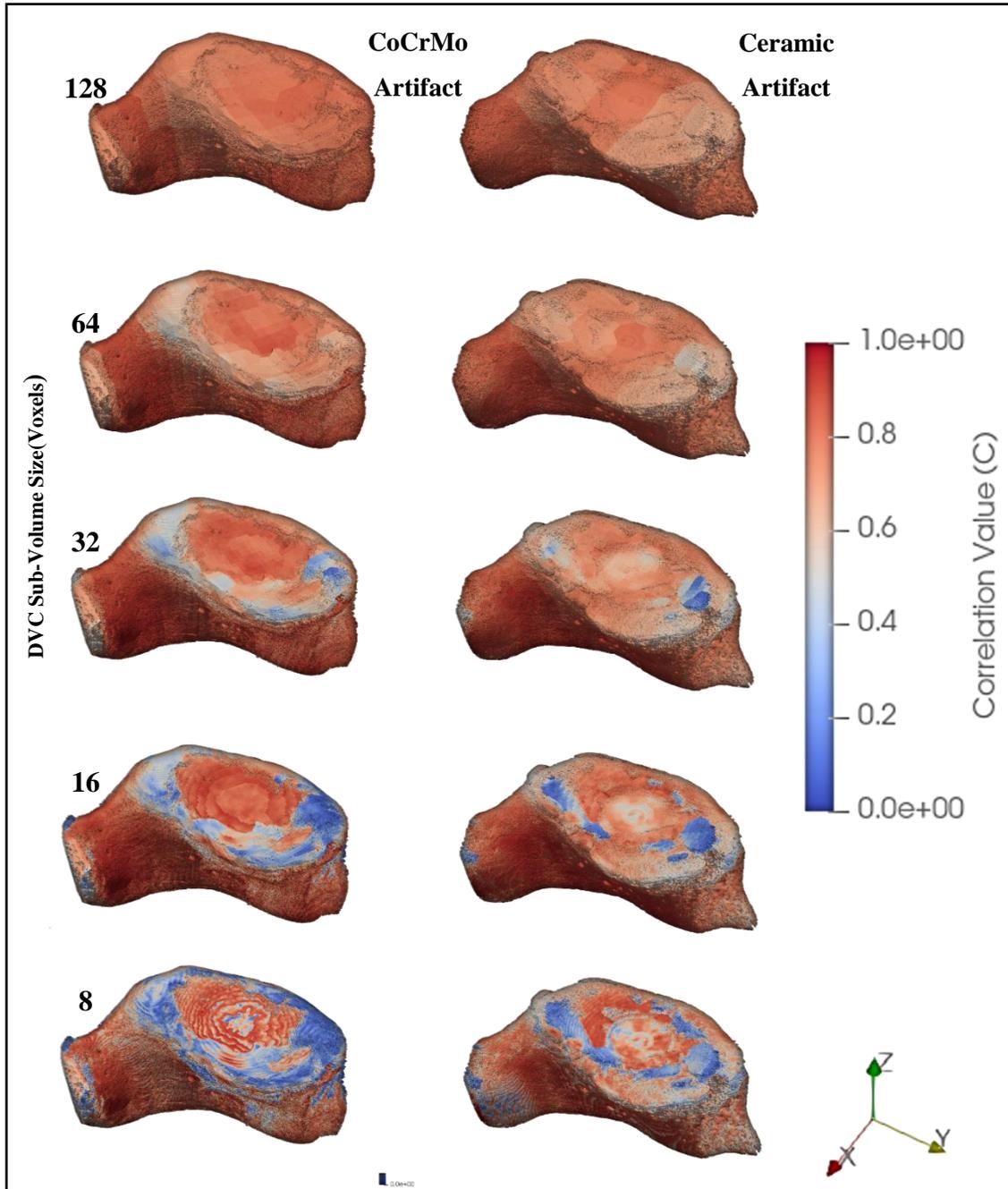
Figure 13: Correlation values overlaid on the glenoid region of interest. As the sub-volume sizes decrease correlation value decrease near the glenoid rim as the slices in this region contain more of the humeral head implants.
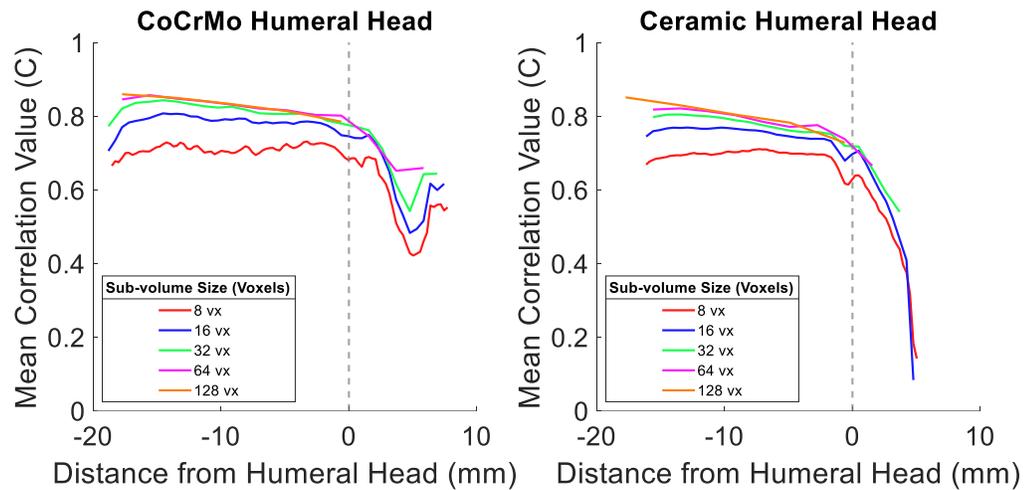
Figure 14: Correlation values as a function of distance from first slice containing the humeral head implant. Correlation values decline slightly in the slices prior to the presence of the artifact inducing material or exhibit no change, and then significantly decline in the slices containing the humeral head implant. Table 3 enumerates the exact location of the beginning of the decline**.** Coordinate system is as described in Fig. 11.

Table 3. Distance at which artifact begins to affect DVC correlation values. Localizing the beginning of the correlation value decline to the first set of correlation values which are significantly different from the sub-volume layer above and below.

		Beginning of Correlation Decline [mm] (p<0.001)	
Sub-Volume Size (voxels)	Sub-Volume Size (mm)	CoCrMo Head	Ceramic Head
128	4.2895	-3.2422	-0.5928
64	2.1448	-1.0982	-0.5928
32	1.0724	-1.0982	-0.5928
16	0.5362	-0.5612	-1.1298
8	0.2681	-0.2932	-1.3978
	Mean	-1.2586	-0.8612
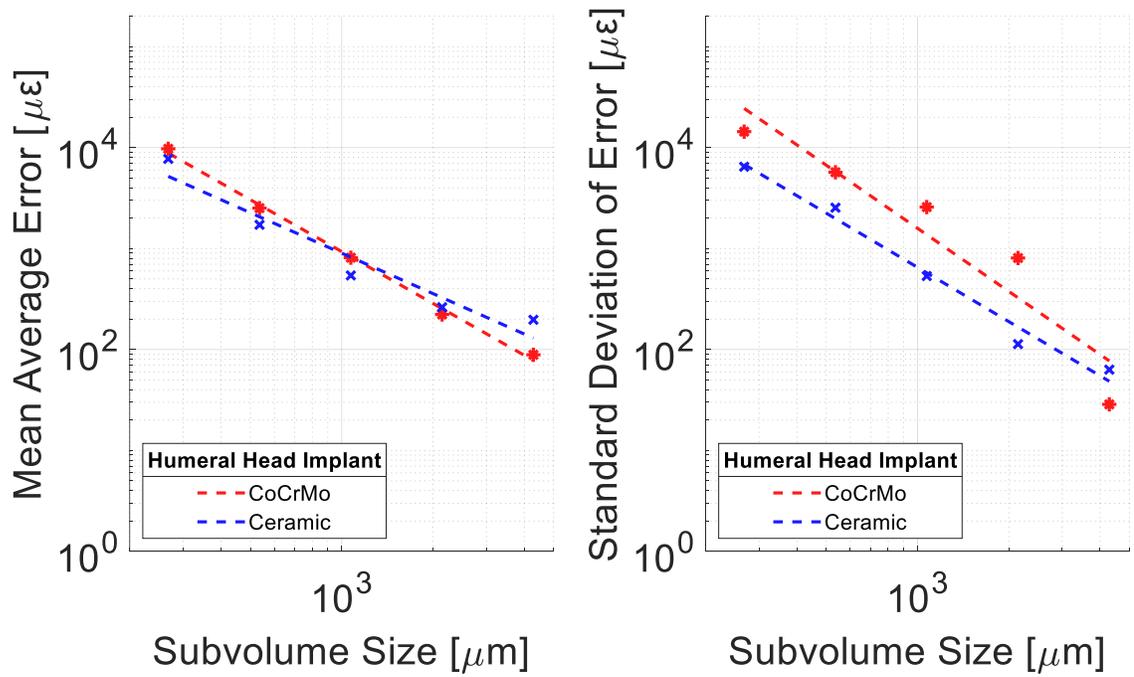
Figure 15: MAE and SDE observed in the CoCrMo head and ceramic head DVC analyses across all sub-volume sizes (8, 16, 32, 64, 128 voxels). MAE values were similar across the range of sub-volumes. SDE values were larger across the range of sub-volume sizes in the CoCrMo humeral head. Power law regressions are displayed with dashed lines.

Table 4. Tabulated DVC MAE and SDE values shown in Fig. 5. without logarithmic adjustment for both humeral head implant materials.

CoCrMo (Sub-volume size, voxels)	MAE (μɛ)	SDE (μɛ)
8	9732	14390
16	2514	5697
32	811.6	2574
64	222.3	806.0
128	88.59	28.61

Ceramic (Sub-volume size, voxels)	MAE (μɛ)	SDE (μɛ)
8	7736	6465
16	1719	2540
32	541.8	534.1
64	262.3	113.1
128	197.0	63.16

Figure 16: Mean absolute error as a function of distance from first slice containing the humeral head implant. The mean absolute error increases slightly in the slices prior to the presence of the artifact inducing material or exhibit no change, and then significantly increase in the slices containing the humeral head implant. The table below enumerates the exact location of the beginning of the increase in MAE. Coordinate system is as described in Fig. 11.

Table 5. Distance at which artifact begins to affect the mean absolute error. Localizing the beginning of mean absolute error increase to the first set of mean absolute error values which are significantly different from the sub-volume layer above and below.

Sub-Volume Size [voxels]	Sub-Volume Size [mm]	Beginning of Absolute Error Increase [mm] ($p<0.001$)	
		CoCrMo Head	Ceramic Head
128	4.2895	N.S.D.	N.S.D.
64	2.1448	N.S.D.	N.S.D.
32	1.0724	N.S.D.	N.S.D.
16	0.5362	-0.5612	-1.1298
8	0.2681	-0.8292	-0.5928
	Mean	-0.6952	-0.8613

3.4   Discussion

The Dice similarity coefficient analysis revealed that in the vicinity of the humeral head implants, the image artifacts that the CoCrMo alloy and alumina-toughened zirconia cause may have a deleterious effect on both the trabecular and cortical bone structure captured in the CT imagery. There was a decline in Dice similarity coefficient beginning ~15-20 mm beneath the humeral head implant in all volumes as compared to the reference volume of the glenoid, with a maximum decrease to 0.605 from 0.847 in the ceramic humeral head imagery and a maximum decrease to 0.658 from 0.817 in the CoCrMo humeral head imagery. The Dice similarity coefficient also rapidly dropped to zero in the glenoid rim of all four volumes indicating no common area between the reference osseous structure and the artifact-affected bone, which was consistent with the observation of a large amount of speckle noise, streaking artifacts and generally poor image quality in this region.

However, at a distance of ~2.5mm from the first slice containing either humeral head, the Dice similarity coefficient began to rise again to a level similar to its maximum value in the region below the humeral head implant. It is difficult to pinpoint the exact cause: it is possible that because the cortical bone at the articular surface of the glenoid encompasses

almost the entire field of view, almost every pixel in the slice is selected for in both the reference image and artifact-containing image, causing a large amount of common area that is bounded by the field of view. Another alternative is that as only the ends of the cadaveric scapula are fixed, one at the medial boundary in the vice of the loading fixture, and the other at the glenoid under the alignment load of 10N, there was some random small relative motion between these constraints, causing large common areas at both ends of the fixation, but variation in position between the fixed ends. The approximate distance between the medial border and the glenoid cavity of the scapula was 10cm, and the Dice coefficient was only calculated for a ~4 cm region from the articular surface of the glenoid, so it is unclear whether this was a major driver of the decline. Another contributing factor could be the imperfect rigid-body registration of the reference scapula to the artifact-containing imagery of the scapula. As the CT image acquisition times were long, inadequate hydration and rehydration of the cadaveric tissue before and between image acquisitions could cause minor expansion and contraction of the scapula, causing the reference scapula to be slightly structurally different from the same scapula as imaged afterwards.

The relationship between DVC correlation value and distance from the artifact-inducing material yielded a more conclusive result. As shown in Fig. 4, there was a clear decline in the mean sub-volume layer correlation value in the region approaching the humeral head. This decline began at a mean distance of 1.26mm and 0.86mm in the CoCrMo humeral head and ceramic humeral head, respectively. The observation that the artifacting effect of the CoCrMo head affected more of the image at a greater distance may be consistent with the knowledge that x-ray attenuation is a function of object density, object thickness, and object atomic properties such as atomic mass and photonic interaction cross-section. The combination of these properties in the CoCrMo head would lead to more significant attenuating effects at constant imaging parameters, leading to photon starvation and beam hardening in the regions where photons transit the CoCrMo humeral head from source to sensor. At the smallest sub-volume size, the distance at which the decline began was significantly different: 0.29mm and 1.40mm in the CoCrMo humeral head and ceramic humeral head, respectively ($p<0.001$). As the sub-volume size becomes smaller, the spatial resolution of the DVC analysis performed becomes correspondingly better—

therefore, these values are potentially good indicators of where the artifact begins to affect the DVC measurements made. The mean distances at which the correlation values decline could also be used as a conservative estimator of the beginning of the glenoidal region affected by the image artifacts. On the basis of the mean correlation value decline reported here, DVC strain measurements made in the glenoid within ~1.5mm of a CoCrMo humeral head and ~1mm of an alumina-toughened zirconia humeral head are likely to be suspect.

In terms of the relationship between the absolute error and distance from the articular surface, the magnitude of error was not pronounced in the larger sub-volume sizes, i.e. there was no significant difference in the sub-volume inter-layer error across 128, 64, and 32 voxel sub-volumes. At the smallest sub-volume size of 8 voxels, the distance at which the error was first significantly different was 0.59mm and 0.83mm in the ceramic and CrCoMo head, respectively. This falls below the conservative estimator suggested above. As far as the author could determine, there have been no investigations into the depth of the regions of the glenoid implicated to be involved in accelerated glenoid wear in hemiarthroplasties, only retrospective analyses of the anatomic extent of glenoid erosion. Nonetheless, the quality of the DVC strain measurements beyond those depths are likely to be sound and can be used to evaluate the difference in strain distributions associated with different humeral head materials *in vitro*.

In terms of the measurement error, at the sub-volume size of 32 voxels recommended previously in 33.5 μm isotropic voxel size imagery, the (MAE, SDE) were (811.6, 2574) με and (541.8, 534.1) με, for the CoCrMo humeral head and ceramic humeral head, respectively. Previously, we found that DVC measurements in the glenoid without the presence of artifact at a similar CT slice thickness had a MAE and SDE on the range of (118.3-180.3, 96.2-127.6) με. This represents a large increase in the measurement uncertainty in the presence of the artifacting materials, and it would be perhaps more appropriate to use a sub-volume size of 64 or 128 voxels when performing DVC measurements in the glenoid with humeral head implants of high density and atomic number.

3.5   Conclusion

DVC-based strain measurements can be used to conduct *in vitro* investigations into the role of glenoid strain distributions and material selection in glenoid erosion for hemiarthroplasties. At a sub-volume size of 64 voxels (2184μm), the observed DVC measurement uncertainty as denoted by the (MAE, SDE) was (222.3, 806.0) με and (262.3, 113.1) με for a CoCrMo humeral head and alumina-toughened zirconia humeral head, respectively. The yield failure of bone trabeculae has a wide range: 7000-40000 με, depending on whether it is a local or apparent-level strain, or compressive or tensile strain[11–14]. The DVC measurement error in the presence of artifact-inducing materials represent only a fraction of this value, and therefore can provide meaningful measurements in this situation. However, there is a site-dependence that also needs to be considered: mean correlation values significantly drop at a mean distance of 1.26mm and 0.86mm in the CoCrMo humeral head and alumina-toughened zirconia humeral head, respectively. The mean absolute error of the measurements began to significantly grow at a mean distance of 0.70mm and 0.86mm from the CoCrMo humeral head and alumina-toughened zirconia humeral head. Based on these results, a conservative minimum distance of 1.5mm and 1mm from the articular surface can be used as a guideline at which glenoid DVC-based strain measurements become suspect in the presence of CrCoMo and alumina-toughened zirconia humeral heads.

3.6　References

1.　Barrett JF, Keat N. Artifacts in CT: Recognition and avoidance. *Radiographics*. 2004;24(6). doi:10.1148/RG.246045065

2.　Meinel FG, Bischoff B, Zhang Q, Bamberg F, Reiser MF, Johnson TRC. Metal artifact reduction by dual-energy computed tomography using energetic extrapolation: A systematically optimized protocol. *Investigative Radiology*. 2012;47(7):406-414. doi:10.1097/RLI.0B013E31824C86A3

3.　Boas FE, Fleischmann D. Evaluation of two iterative techniques for reducing metal artifacts in computed tomography. *Radiology*. 2011;259(3):894-902. doi:10.1148/RADIOL.11101782/ASSET/IMAGES/LARGE/101782FIG06B.JPEG

4.　de Man B, Nuyts J, Dupont P, Marchal G, Suetens P. Metal streak artifacts in X-ray computed tomography: a simulation study. *IEEE Nuclear Science Symposium and Medical Imaging Conference*. 1999;3:1860-1865. doi:10.1109/NSSMIC.1998.773898

5.　Rodrigues SP, Paiva JM, de Francesco S, Amaral MI, Oliveira FJ, Silva RF. Artifact level produced by different femoral head prostheses in CT imaging: Diamond coated silicon nitride as total hip replacement material. *Journal of Materials Science: Materials in Medicine*. 2013;24(1):231-239. doi:10.1007/S10856-012-4778-0/FIGURES/8

6.　Klawitter JJ, Patton J, More R, Peter N, Podnos E, Ross M. In vitro comparison of wear characteristics of PyroCarbon and metal on bone: Shoulder hemiarthroplasty. *Shoulder & Elbow*. 2020;12(1 Suppl):11. doi:10.1177/1758573218796837

7.　Herschel R, Wieser K, Morrey ME, Ramos CH, Gerber C, Meyer DC. Risk factors for glenoid erosion in patients with shoulder hemiarthroplasty: an analysis of 118 cases. *Journal of Shoulder and Elbow Surgery*. 2017;26(2):246-252. doi:10.1016/J.JSE.2016.06.004

8.　Parsons IM, Millett PJ, Warner JJP. Glenoid Wear after Shoulder Hemiarthroplasty. *Clinical Orthopaedics & Related Research*. 2004;421:120-125. doi:10.1097/01.BLO.0000119249.61696.F1

9.   Barret H, Gauci MO, Langlais T, van der Meijden O, Tran L, Boileau P. Pyrocarbon interposition shoulder arthroplasty in young arthritic patients: a prospective observational study. *Journal of Shoulder and Elbow Surgery*. 2020;29(1):e1-e10. doi:10.1016/J.JSE.2019.05.044

10.   Hannoun A, Ouenzerfi G, Brizuela L, et al. Pyrocarbon versus cobalt-chromium in the context of spherical interposition implants: An in vitro study on cultured Chondrocytes. *European Cells and Materials*. 2019;37:1-15. doi:10.22203/ECM.V037A01

11.   Morgan EF, Keaveny TM. Dependence of yield strain of human trabecular bone on anatomic site. *Journal of Biomechanics*. 2001;34(5):569-577. doi:10.1016/S0021-9290(01)00011-2

12.   Odgaard A, Hvid I, Linde F. Compressive axial strain distributions in cancellous bone specimens. *Journal of Biomechanics*. 1989;22(8-9):829-835. doi:10.1016/0021-9290(89)90066-3

13.   Bayraktar HH, Morgan EF, Niebur GL, Morris GE, Wong EK, Keaveny TM. Comparison of the elastic and yield properties of human femoral trabecular and cortical bone tissue. *Journal of Biomechanics*. 2004;37(1):27-35. doi:10.1016/S0021-9290(03)00257-4

14.   Nagaraja S, Couse TL, Guldberg RE. Trabecular bone microdamage and microstructural stresses under uniaxial compression. *Journal of Biomechanics*. 2005;38(4):707-716. doi:10.1016/J.JBIOMECH.2004.05.013

4 An *in vitro* Study of Glenoid Implant Peripheral Peg-Cement-Bone Interface Mechanics Under Simulated Glenoid Lift-Off Loading

OVERVIEW

Glenoid implants used in total shoulder arthroplasties to treat glenohumeral osteoarthritis incorporate peripheral pegs as a common design feature to support eccentric loads. These peripheral pegs and the implant-cement-bone interface that they constitute undergo substantial cyclic tensile-compressive loads due to the rocking horse effect: the observation that glenoidal loads cyclically vary from the superior to the inferior edge of the glenoid *in vivo*. These pegs are of interest in translating the micromechanics of local implant fixation failure to the biomechanics of gross anatomic failure of the glenoid implant after total shoulder arthroplasty. This study uses an *in vitro* recovered tissue model of glenoid implant peripheral pegs using osteoarthritic patient bone to analyze strain patterns in the peripheral peg-cement-bone interface.

4.1 Introduction

In total shoulder arthroplasty the glenoid implant component is a critical design consideration as aseptic glenoid implant loosening remains the largest single reason for failure.[1,2] The rocking horse mechanism, whereby cyclic eccentric glenoid loading is thought to drive progressive failure of the cement mantle of the glenoid, is thought to be the cause of glenoid loosening in the absence of any other pathological mechanism.[3] As the resultant joint forces progress from the inferior to the superior glenoid edge *in vivo*, the loading of the edge of the glenoid causes significant stresses in the fixation under the edge of the glenoid implant, and lift-off on the opposite edge.[4] There are multiple glenoid implant designs available on the market; in cemented fixation, a commonly seen design feature is a large central press-fit peg flanked by smaller diameter pegs located at the superior and inferior aspects of the glenoid. The role of these peripheral pegs is to support the glenoid edge loads that are generated in the rocking horse mechanism.[5]

The progressive failure of the implant-cement-bone interface is not well understood: though the rocking horse mechanism is an overarching explanation of the loads experienced and the global failure of the glenoid implant, the local dynamics of the failure of the interface and critical locations have not been made clear.[6] A candidate for the beginning of failure are the interfaces surrounding the superior/inferior pegs as the joint reaction force varies from the superior to the inferior aspect of the glenoid causing a cyclic compressive-tensile load in these pegs. Polymethyl-methacrylate bone cement is a material that is brittle and asymmetric, being significantly weaker in tension than in compression. Therefore, the cyclic compressive-tensile loads that are experienced by the pegs supporting the glenoid implant rim may initiate the damage to the implant-cement-bone interface which ultimately causes glenoid failure by eliciting high tensile loads in the weak-in-tension PMMA bone cement.[7] The magnitude of the loads experienced by the superior and inferior pegs have been investigated in FEA models of certain glenoid implant designs, but, to the authors knowledge, an *in vitro* investigation of the forces generated under the glenoid pegs and the corresponding mechanical response of the peg-cement-bone interface through digital volume correlation has not been performed.[5,8]

This study employs a custom-designed radiolucent testing fixture and patient-specific end-stage osteoarthritic bone to investigate the load transfer underneath a glenoid implant peripheral peg. It leverages the combination of micro-CT imagery and digital volume correlation strain measurements to examine the behaviour of the implant-bone-cement interface by simulating the lift-off displacements experienced by glenoid implants *in vivo* and measuring the maximum and minimum principal strains in critical locations around a glenoid implant peripheral peg.

4.2   Methods

4.2.1   Specimen Preparation

Ten humeral osteotomies were recovered post-resection from total shoulder arthroplasty procedures. They were subsequently wrapped in phosphate buffered saline-soaked gauze and frozen until specimen preparation. The humeral osteotomies were cored using a 0.5" diamond-burred hole saw perpendicular to the resection surface at the highest point of the

bone surface. The bone cores were then cut to a length of 20mm using a low speed wafer saw by resecting the requisite length from the side of the osteotomy resection plane if the cores were longer than 20mm. Cores shorter than 16mm were not used. The cores were then potted in a PLA 3D receptacle using PMMA bone cement after positioning them in the center of the receptacle using a 3D printed pilot. The PMMA was mixed according to manufacturer instructions. a 7/32" hole was drilled in the core to a depth of 10mm using a 3D printed pilot to guide the drill to the centre of the core. A 4mm diameter peg (Fig. 17) was cemented into the drilled hole using PMMA bone cement. The specimens were then frozen for storage.
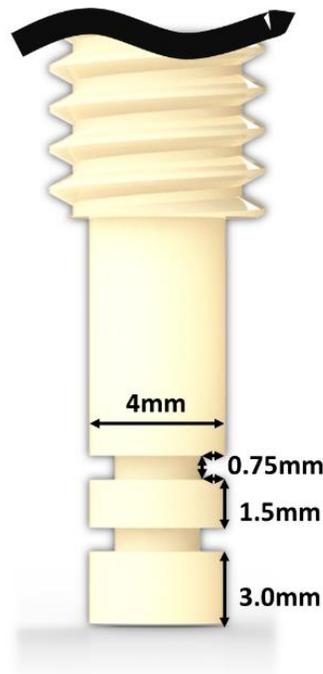
Figure 17: Critical dimensions and geometry of peripheral peg used in loading.

4.2.2 Loading Protocol and Imaging

Specimens were thawed and placed into a custom-designed radiolucent loading fixture emplaced within a 6-DOF Stewart platform robot (Fig. 18) (Picard Industries, Albion, NY, USA). The robot was then placed into a cone-beam micro-CT scanner (XTH 225ST, Nikon, Minato, Japan) and fixed into place on the micro-CT rotating imaging platform. A

micrometer-adjustable X-Y stage was included in the robot fixturing for ease of adjusting the robot and sample position relative to the center of rotation of the rotating platform. 10 (n=10, age: 70.9 years±10.8 years, 5 male and 5 female) osteoarthritic bone specimens were randomly assigned to either a primarily tensile or primarily compressive loading protocol. After randomization, the tensile group contained 5 (n=5, age=68.8 years±7.1 years, 2 male and 3 female) specimens and the compressive group contained 5 (n=5, age=73.0 years± 11.8 years, 3 male and 2 female) specimens. In order to generate glenoidal loads which are representative of what is experienced *in vivo* as through the rocking horse mechanism, a point was digitized on the superior and central peg of a glenoid implant model. A coordinate system based on the base of the central peg of the glenoid implant was created, and the base of the specimen peg was either rotated in a positive or negative direction around that coordinate system (Fig. 19). For the primarily-tensile loading, images of the specimens were captured in an unloaded state and at 1 degree increments of rotational displacement up to a level of 4 degrees. For the primarily-compressive loading, images of the specimens were captured in an unloaded state and at 1 degree increments of rotational displacement up to a level of 3 degrees. (Fig 19). Micro-CT imaging parameters were as follows: (1571 projections, 1000ms exposure, 80mA, 120 kVp, 12μm isotropic voxel size,). A load cell (nano 25, ATI Industrial Automation, Apex, NC, USA) was instrumented beneath the loading apparatus in order to measure the loads exerted on the bone core.
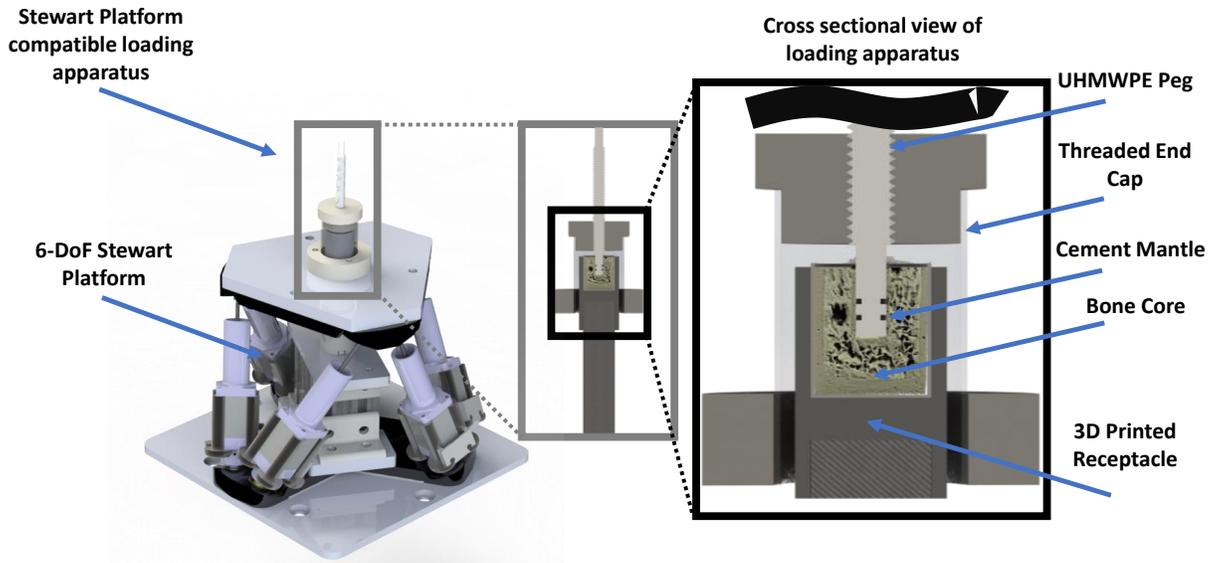
Figure 18: Cross sectional view of the loading apparatus, bone core, peripheral peg and their integration into the Stewart platform used for loading.

4.2.3   Image Processing and DVC Analysis

The micro-CT images were converted from 32-bit floating point attenuation value volumetric images to 16-bit greyscale images using Dragonfly (Object Research Systems, Montreal, Canada). A thresholding operation was performed to segment the PMMA cement and bone core trabecular structure, with the threshold value being consistently applied between separate volumes. A 6-connectivity region growing operation removed spurious noise and detached elements from the cement-bone structure. Voxels which did not correspond to either cement or bone were set to a greyscale value of 0, and the images were converted to 8-bit greyscale. The images were then imported to DaVis, a commercially available proprietary DVC software package, and DVC analysis was performed on the loaded imagery relative to the unloaded image captured. DaVis-DVC uses a hybrid DVC approach, with a first approximation of a solution being found through a pass of a FFT-DVC algorithm, and then iteratively approaching a solution through a series of decreasing sub-volume size passes using a global-DVC algorithm. The DVC parameters were as follows: (sub-volume size: 16 voxels, valid voxel requirement: 50%, FFT pre-shift window size: 128 voxels, peak search: 8 or 16 voxels.)
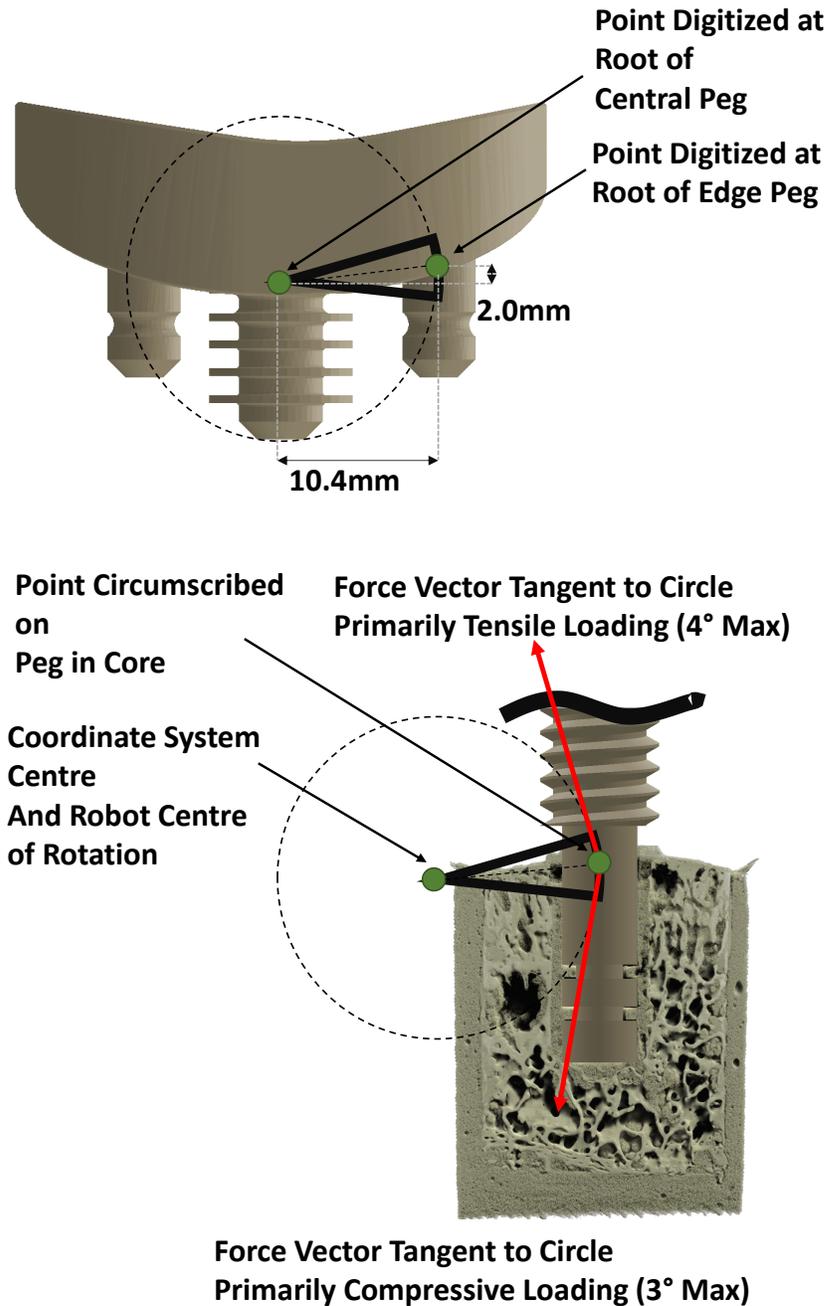
Figure 19: Loading Protocol and coordinate system digitization with respect to the glenoid implant design used. Note that the geometry of the peg was not emulated, only the implant dimensions.

4.2.4   Regions of Interest and Statistical Analysis

From the DVC analysis, two regions of interest were identified. The first corresponded to the region ≤1mm away from the peg, and contained a combination of trabecular bone and PMMA bone cement. corresponded to the region >1mm away from the peg and was primarily occupied by trabecular bone. In these two regions, four transverse planes were identified as being of particular interest to quantify the behaviour of the peg-cement-bone interface. The highest maximum principal strains and lowest minimum principal strains as measured by DVC were extracted in both of the regions of interest corresponding to each plane. The planes were defined relative to the surface of the core and by key geometric features of the peg. The first plane corresponded to the bone 2mm from the core surface, and contained the transitional trabeculae underneath the cortical surface of the core. The second plane corresponded to the midpoint between the first plane and the beginning of the channels in the peg geometry. The third plane corresponded to the axial midpoint of the peg between the two channels, and the fourth plane corresponded to the region directly below the peg (Fig. 21).

A 4-way ANOVA was performed on the data set, with the independent variables being the degree of displacement, the plane of measurement, whether the strain measured was the maximum or minimum principal strain, and the region of interest to which the measurement corresponded. For the purpose of the analysis, these variables were assumed to be independent of one another. Pearson correlations between the maximum compressive/tensile and lateral force, and morphometric parameters of bone (BV/TV, Tb. Th., Tb. Sp. Tb. N.) were also investigated. Bone morphometric parameters were calculated by isolating a virtual cylinder of bone from the segmented imagery that excluded cement and ran the height of the bone core in order to obtain an average sample of the condition of the bone from the sub-cortical trabeculae to the trabeculae near the bottom of the core. The image stack corresponding to this virtual cylinder was exported and analysed using CTAn.

Bone Cores Assigned to Primarily Tensile Loading

Core Dimensions 0.5"

Bone Cores Assigned to Primarily Compressive Loading

20mm
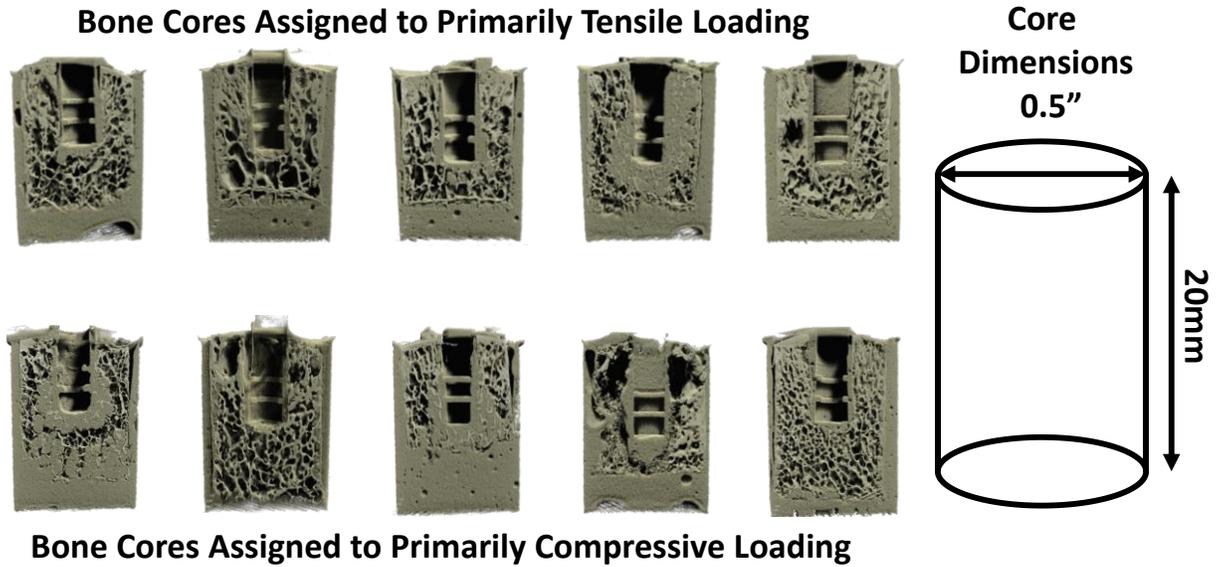
Figure 20: 3D render of cross-sectional view of bone core trabecular structure and bone cement after 3D volumetric image segmentation. Of note is the variable amount of cement that permeates the trabecular structure from the peg outwards.
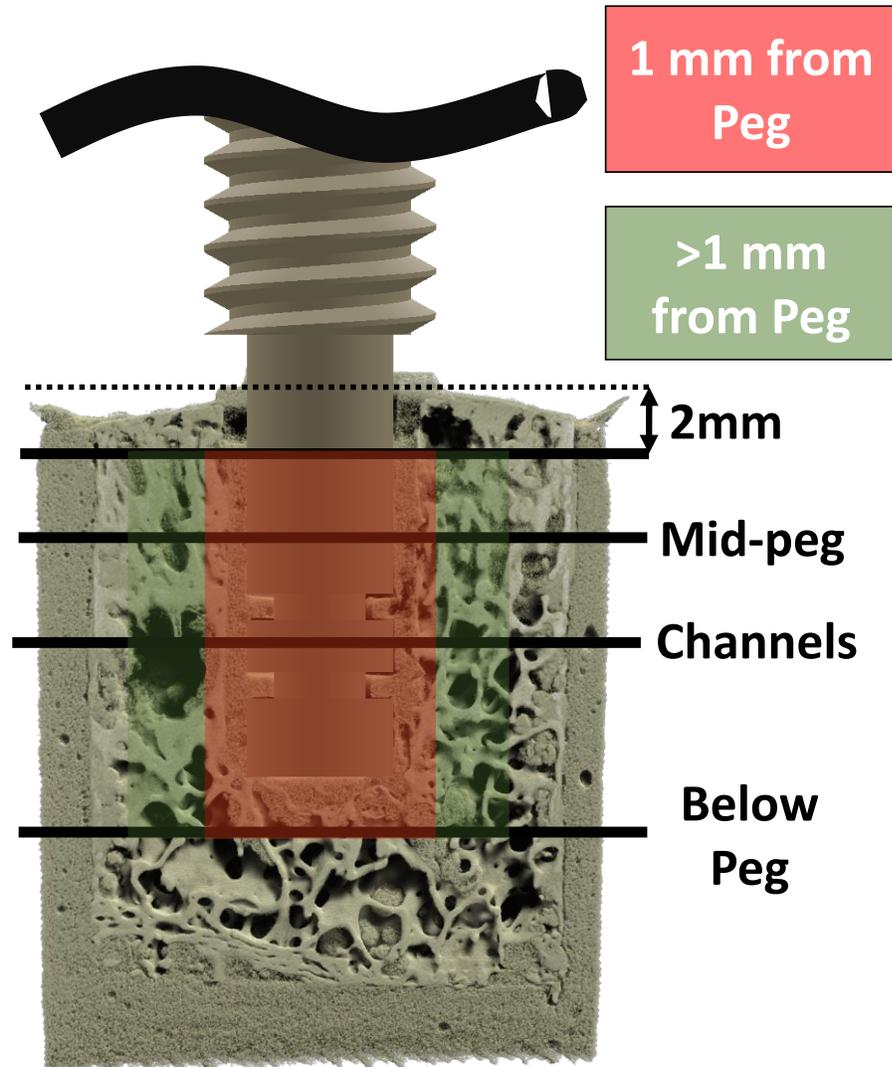
Figure 21: The two regions of interest highlighted in red (region closest to peg) and green (region >1mm away from the peg) alongside the four planes of measurement as they descend along the length of the peg. This leads to 16 unique strain measurements per core per level of rotational displacement: a maximal maximum principal strain and minimum principal strain in each region of interest at every plane of measurement.

4.3   Results

Table 6: Bone core specimen morphometric parameters.

Specimen	BV/TV (%)	Tb. Th. (mm)	Tb. Sp. (mm)	Tb. N. (1/mm)
1-Tension	26.2	0.184	0.579	1.425
2-Tension	29.6	0.242	0.701	1.22
3-Tension	19.1	0.166	0.687	1.148
4-Tension	20.0	0.154	0.540	1.299
5-Tension	34.6	0.265	0.570	1.305
6-Compression	21.0	0.148	0.588	1.415
7-Compression	37.9	0.280	0.569	1.353
8-Compression	32.2	0.305	0.965	1.055
9-Compression	30.0	0.220	0.609	1.361
10-Compression	29.8	0.189	0.471	1.571

Table 7: Measured mean loads at each level of rotational displacement for both the primarily tensile and primarily compressive loading. (± 1 S.D.)

		Displacement [°]			
Loading		**1**	**2**	**3**	**4**
Tension	**Mean Lateral Force [N]**	5.37±2.70	8.31±3.77	16.38±6.46	17.93±7.53
	Mean Axial Force [N]	33.24±10.0	53.77±14.3	66.76±14.5	76.56±11.1
Compression	**Mean Lateral Force [N]**	3.14±1.37	5.76±1.46	17.85±9.47	N/A
	Mean Axial Force [N]	34.70±15.5	65.99±17.9	83.82±5.73	N/A
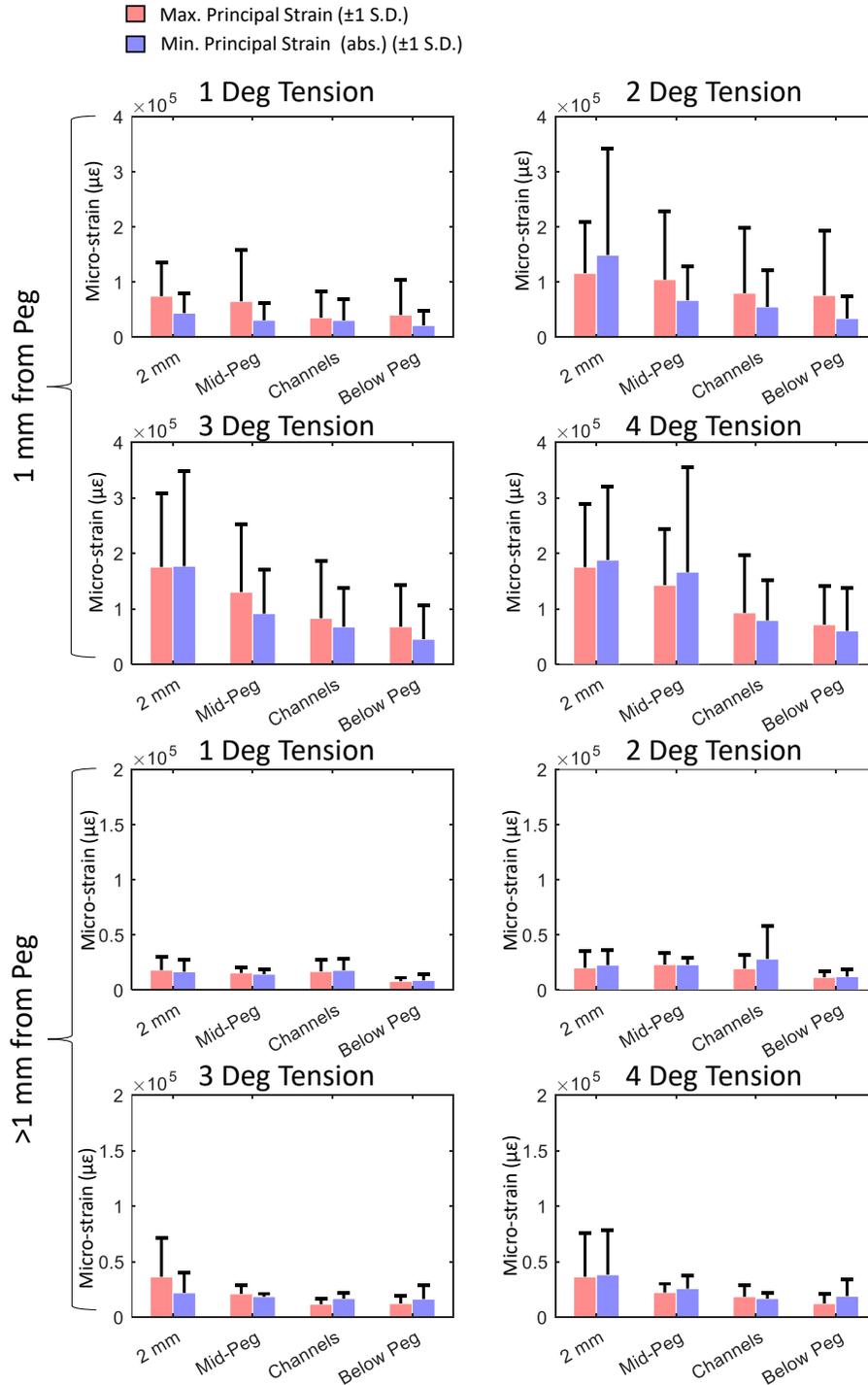
Figure 22: Mean maximum and minimum principal strains measured in the regions of interest shown in Fig. 16 under the primarily tensile loading conditions. Significant effects are described in 4.3.1.
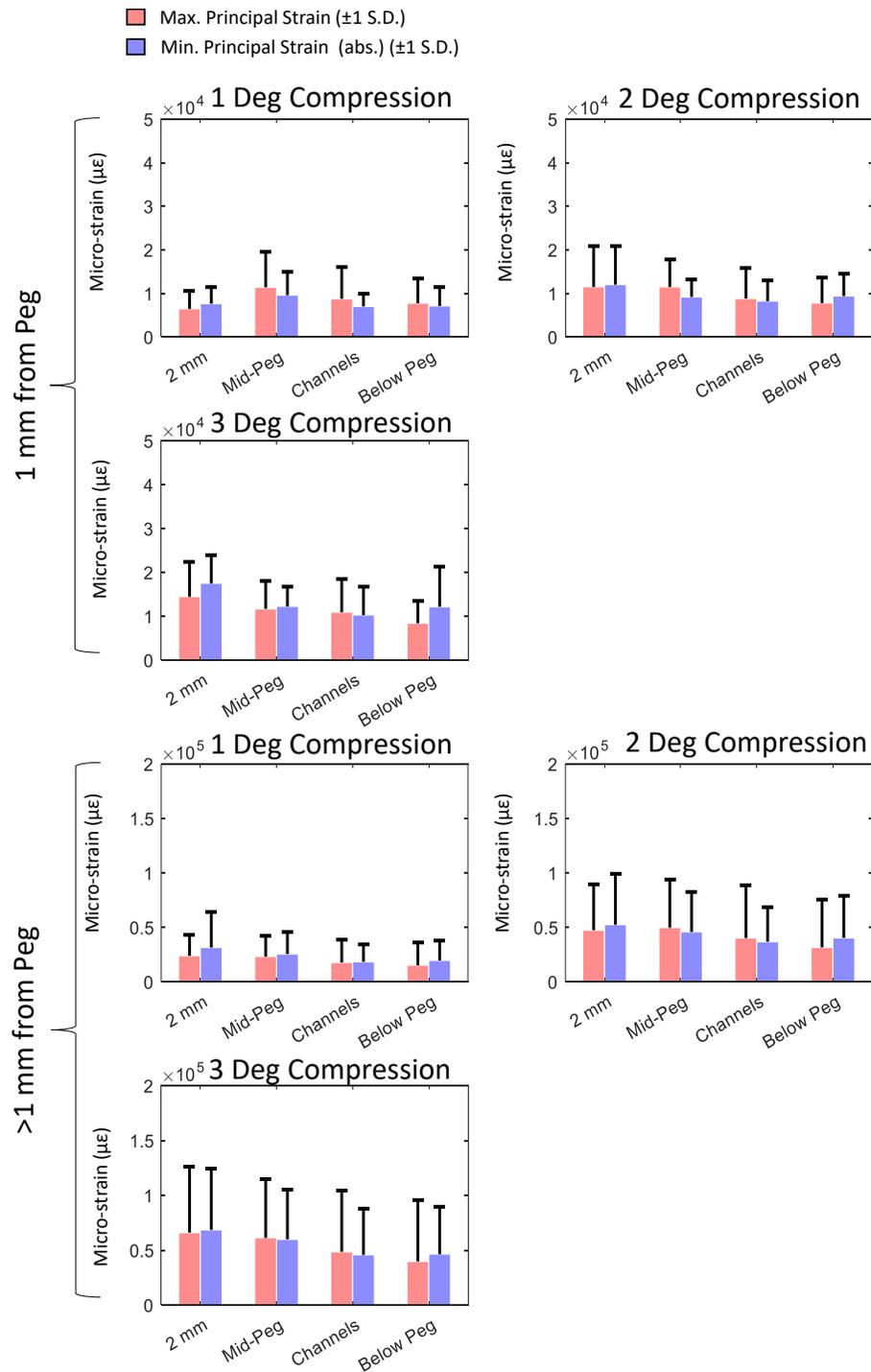
Figure 23: Mean maximum and minimum principal strains measured in the regions of interest shown in Fig. 16 under the primarily compressive loading conditions. Significant effects are described in 4.3.1.

Table 8: Significant correlations between maximum forces experienced by bone cores and bone morphometric parameters. Only correlations under the tensile loading condition were found to be significant.

Significant Correlations in Primarily Tensile Loading (p<0.05)		
Max. Tensile Force	**BV/TV**	r(3)=0.9004, p=.0372
BV/TV	**Tb. Th.**	r(3)=0.8221, p=.0477
Max. Tensile Force	**Tb. Th.**	r(3)=0.9836, p=.0025

4.3.1   Statistical Analysis (4-way ANOVA and post-hoc tests)

In order to allow for comparison between the maximum and minimum principal strains, the absolute value of the minimum principal strain was used in the statistical analysis performed. For the primarily tensile loading, the 4-way ANOVA revealed that there was a significant effect between at least two groups of the measurement plane on the measured strain (F(3)=7.642, p<.001). It also found there to be a significant effect between at least two rotational displacements and the measured strains (F(3)=5.558, p=.001). Interestingly, there was no statistically significant difference in the magnitude of the maximum and minimum principal strains (F(1)=.674, p=.412). There was also a significant difference between region 1mm from the peg and the region >1mm from the peg (F(1)=75.281, p<.001).

There was found to be significant effect in the plane of measurement-distance from peg interaction on the measured strain (F(3)=4.206, p=.006). There was also found to be a significant effect in the rotational displacement-distance from peg interaction on the measured strain (F(3)=3.665, p=.013).

A post-hoc Tukey test performed on the partial effect of measurement plane found there to be a significant difference between the strains measured 2mm below the cortical shell and all other groups except the strains measured mid-peg. (2mm-channels p=0.003, 2mm-

below peg p<.001). A post-hoc Tukey test performed on the partial effect of rotational displacement found there to be a significant difference in the strains measured at 1 degree of rotational displacement 3-4 degrees of rotational displacement. (1-3 p=0.019, 1-4 p<.001)

For the primarily compressive loading, the 4-way ANOVA revealed there was a significant effect between at least two rotational displacements and the measured strains (F(2)=8.102, p<.001). There was also a statistically significant difference the strains measured 1mm from the peg and >1mm from the peg (F(1)=63.227, p<.001). There was a significant effect between the interaction of rotational displacement and the distance from the peg on the measured strains (F(2)=5.074, p=.007). Interestingly, no other effects were found to be significant or near significance. Again, the magnitude of maximum and minimum principal strains were not found to be statistically significant.

A post-hoc Tukey test on the partial effect of rotational displacement found that the strains measured at 1 degree of rotational displacement were significantly different from the strains measured at 2-3 degrees of rotational displacement (1°-2°p=.038, 1°-3° p<.001). The difference between 2 degrees and 3 degrees of rotational displacement was not significant (p=0.288).

Correlations between the maximum lateral force, maximum compressive/tensile force, BV/TV, Tb. Th., Tb. Sp. and Tb. N. were calculated. Only 3 were found to be significant as noted in Table 8. All of these correlations were found in the primarily tensile loading with no significant correlations appearing between any of these parameters in the primarily compressive loading.

4.4   Discussion

The region of interest <1mm away from the peg features the interaction of the interface of the peg with the PMMA bone cement and the trabecular structure. The strains measured here were significantly larger than those >1mm away from the interface at all levels of displacement, as seen in Figs. 22-23. As a representative example, at 4 degrees of rotational displacement in the primarily tensile loading and in the measurement plane

2mm from the peg surface, the mean values of ε_1 and ε_3 were 1.75e5 $\mu\varepsilon$ and 1.88e5 $\mu\varepsilon$, respectively in the near peg-cement-bone interface region. Comparatively, the mean values of ε_1 and ε_3 in the region >1mm away from the peg were 3.64e4 $\mu\varepsilon$ and 3.83e4 $\mu\varepsilon$. This constitutes just under an order of magnitude difference in strain magnitude. As bone cement does not adhere to either the implant or bone, instead acting as a kind of grout in orthopedic applications, micro-displacement or slippage between any constituent components of this interface could potentially be resolved at the length scale of micro-CT imagery. [9] Both the cement and bone were included in the segmented imagery; the high strains at the interface likely do not constitute internal strains of any individual member of the interface, rather, they represent the strain that would be measured if the bone and cement were to be treated as one body. As the bone cement experiences some displacement and the bone remains in place, albeit as a deformed body, the measurement of total deformation of the sub-volumes will be high as the DVC analysis does not differentiate between bone cement and trabecular bone. This still reveals interesting properties of the behaviour of the interface itself. If a failure criterion as a function of these strains could be developed from treating this these two individual components as a whole body, these internal strains could be used to delineate between likely points of failure and acceptable levels of strain. As the distance from the cement was increased, the trabeculae directly attached to the trabeculae interfacing with the cement still experienced high strains—with some measured strains being higher than reported physiological trabecular strain failure values of 7000-40000 $\mu\varepsilon$, which may indicate trabecular failure proximal to the implant-cement interface in loading that simulates what is experienced *in vivo*. [10–13] In future analyses, a treatment that performs a DVC analysis on the cement and bone separately as well as together could shed more light on the internal mechanical behaviour of the individual components of the interface as well as their combined mechanical behaviour.

Another effect that was seen in the primarily tensile loading was the effect of plane of measurement on the level of strain. As the measurement plane proceeded downwards axially along the peg, the mean minimum and maximum principal strain both <1mm and >1mm away from the peg decreased. This effect was not seen in the primarily

compressive case. This could mean regions of interest for analyses of failure could focus on the peg-cement-bone interface proximal to the implant.

In order to facilitate the comparison of the maximum and minimum principal strains, the absolute values of the minimum principal strains measured were used in the statistical analysis. In both the primarily compressive and tensile loading, there was found to be no significant difference between maximum and minimum principal strains. The apparent symmetry between minimum and maximum principal strains may again indicate that a tensile failure is the failure mode worth examining in further detail in the cement mantle of superior pegs of glenoid implants, an observation paralleled both in finite element studies and *in vitro* cadaveric studies of the glenoid implant-cement-bone interface. On the DVC measurement length scale of 192 µm used in these analyses, these high tensile strains may indicate high tensile stresses in critical geometries of the cement mantle (i.e. areas filled in between trabeculae where the cross sectional area narrows) which may cause local failure, crack initiation in the cement mantle and ultimately leading to global failure after many cycles of cyclic loading.

There were important limitations to this study that should temper the insights gleaned therein. Only 5 cores were assigned to each set of loading conditions; this low sample size could induce spurious correlations—purportedly strong coefficients of correlation such as those seen in the correlations between the maximum tensile force and BV/TV could diminish with increasing sample size. An increase in sample size could also improve the breadth of the strain measurements, and potentially allow for correlations to be established between the strains experienced in the regions of interest investigated and local bone morphometric parameters. Though the PMMA used in this study was mixed according to manufacturer instructions, the methods for mixing cement in the orthopedic operating room are different and more controlled—certain techniques are employed to minimizes the formation of voids and density variations in the PMMA such as vacuum mixing.[14] In the future, emulating these approaches could positively influence the repeatability of these results. Moreover, a consistent amount of cement used between cores could help improve the consistency of the thickness of the cement mantle underneath the pegs. Though in most bone cores included in this study the cement mantle

thickness was close to previously studied values, there were a couple of notable outliers in which the cement penetrated deep into the trabecular structure, causing a mantle that was substantially larger than expected. [6,15] The geometry of the bone cores themselves slightly varied as the plane of resection between humeral osteotomies was not of a consistent distance from the point of articulation on the humeral head, though longer cores were resected to a nominal length of 20mm. The generalizability of these results is difficult to establish as the study only investigated a single peg geometry and glenoid implant dimensions. In the future, comparisons between multiple peg geometries may allow for additional insights. Finally, the bone cores themselves were extracted from humeral osteotomies and not glenoidal tissue. The OA patient specificity of this recovered tissue is a strength, as it represents degraded tissue that the glenoid implant would typically interface with. However, the difference in anatomic site may cause slight differences in bone properties. This can be controlled for at least in part through the reporting of bone morphometric parameters to inform interpretation of these results, as was done in this study.

4.5   Conclusion

This study used osteoarthritic patient-specific tissues to investigate the strain in the glenoid implant peripheral peg-cement-bone interface under conditions simulating glenoid lift-off. It was found that there is a significant relationship between location along the peg and the magnitude of the maximum and minimum principal strains, indicating that regions closer to the glenoid implant articulating surface are more likely to be the site of initial failure. In addition, the trabecular strains in the regions not directly in contact with the bone cement (>1mm away condition) were typically below reported failure values for trabecular strains, again reinforcing the suggestion that cement and trabecular bone regions closest to the implant experience the largest strains and are a likely candidate for the local failure initiation of the glenoid implant-cement-bone interface in total shoulder arthroplasty.

4.6 References

1.   Dines JS, Fealy S, Strauss EJ, et al. Outcomes analysis of revision total shoulder replacement. *Journal of Bone and Joint Surgery - Series A*. 2006;88(7):1494-1500. doi:10.2106/JBJS.D.02946

2.   Bonnevialle N, Melis B, Neyton L, et al. Aseptic glenoid loosening or failure in total shoulder arthroplasty: revision with glenoid reimplantation. doi:10.1016/j.jse.2012.08.009

3.   Matsen FA, Clinton J, Lynch J, Bertelsen A, Richardson ML. Glenoid component failure in total shoulder arthroplasty. *Journal of Bone and Joint Surgery - Series A*. 2008;90(4):885-896. doi:10.2106/JBJS.G.01263

4.   Collins D, Tencer A, Sidles J, Matsen F. Edge displacement and deformation of glenoid components in response to eccentric loading. The effect of preparation of the glenoid bone. *Journal of Bone & Joint Surgery-American Volume*. 1992;74(4):501-507.

5.   Stautberg EF, Jupiter DC, Amin A, Qadeer AA, Ilahi OA. Stability of two versus three peripheral pegs of the glenoid component in modern total shoulder arthroplasty. *International Orthopaedics*. 2017;41(11):2345-2351. doi:10.1007/S00264-017-3599-7/FIGURES/6

6.   Flint WW, Lewis GS, Wee HB, Bryce BJ, Armstrong AD. Glenoid cement mantle characterization using micro–computed tomography of three cement application techniques. *Journal of Shoulder and Elbow Surgery*. 2016;25(4):572-580. doi:10.1016/J.JSE.2015.08.031

7.   Hopkins AR, Hansen UN, Amis AA, Emery R. The effects of glenoid component alignment variations on cement mantle stresses in total shoulder arthroplasty. *Journal of Shoulder and Elbow Surgery*. 2004;13(6):668-675. doi:10.1016/J.JSE.2004.04.008

8.   Wahab AHA, Kadir MRA, Harun MN, Kamarul T, Syahrom A. Number of pegs influence focal stress distributions and micromotion in glenoid implants: a finite element

study. *Medical and Biological Engineering and Computing*. 2017;55(3):439-447. doi:10.1007/S11517-016-1525-6/FIGURES/6

9. Magnan B, Bondi M, Maluta T, Samaila E, Schirru L, Dall'Oca C. Acrylic bone cement: Current concept review. *Musculoskeletal Surgery*. 2013;97(2):93-100. doi:10.1007/S12306-013-0293-9/FIGURES/3

10. Morgan EF, Keaveny TM. Dependence of yield strain of human trabecular bone on anatomic site. *Journal of Biomechanics*. 2001;34(5):569-577. doi:10.1016/S0021-9290(01)00011-2

11. Odgaard A, Hvid I, Linde F. Compressive axial strain distributions in cancellous bone specimens. *Journal of Biomechanics*. 1989;22(8-9):829-835. doi:10.1016/0021-9290(89)90066-3

12. Bayraktar HH, Morgan EF, Niebur GL, Morris GE, Wong EK, Keaveny TM. Comparison of the elastic and yield properties of human femoral trabecular and cortical bone tissue. *Journal of Biomechanics*. 2004;37(1):27-35. doi:10.1016/S0021-9290(03)00257-4

13. Nagaraja S, Couse TL, Guldberg RE. Trabecular bone microdamage and microstructural stresses under uniaxial compression. *Journal of Biomechanics*. 2005;38(4):707-716. doi:10.1016/J.JBIOMECH.2004.05.013

14. Gergely RCR, Toohey KS, Jones ME, Small SR, Berend ME. Towards the optimization of the preparation procedures of PMMA bone cement. *Journal of Orthopaedic Research*. 2016;34(6):915-923. doi:10.1002/JOR.23100

15. Nyffeler RW, Anglin C, Sheikh R, et al. Influence of peg design and cement mantle thickness on pull-out strength of glenoid component pegs. *Journal of Bone and Joint Surgery - Series B*. 2003;85(5):748-752. doi:10.1302/0301-620X.85B5.12580

5   Conclusion

OVERVIEW

This conclusory chapter assesses the objectives of this thesis in the context of the studies performed, aggregates their results and significance, and reiterates the individual findings as a function of the overarching significance of the thesis work. Strengths and limitations of this body of work are analyzed, and future directions for each strand of study are outlined on the basis of the findings of the thesis.

5.1   Summary

The goal of this thesis work was to investigate the role of DVC and its potential in understanding the biomechanics of clinical problems in the osteoarthritic glenohumeral joint. The accuracy and precision of DVC when applied to imagery that applies biomechanical testing of this critical interface is not well understood. Chapters 2 and 3 investigated the accuracy and precision of DVC when applied to biomechanical testing of cadaveric scapular specimens which were both subjected to an unloaded state and simple biomechanically relevant loads. Chapter 4 aimed to extend this thesis beyond investigations of accuracy and precision and shift to application of DVC in the context of understanding critical failure locations of glenoid implants, namely, the peripheral peg-cement bone-interface.

With respect to Objective 1, the accuracy and precision of DVC-derived strain measurements in both the keeled and pegged scapulae was quantified a function of both image acquisition time and DVC measurement spatial resolution. At a sub-volume size of 1072 um and at 1570 CT projections, the highest measurement MAE and SDE were 318 $\mu\varepsilon$ and 1128 $\mu\varepsilon$ respectively, as derived through a zero-strain analysis of measurement error. The loaded analysis found that the highest relative difference and the standard deviation of this relative difference in the measured strains at a sub-volume size of 1072 and at 1570 CT projections to be 689 $\mu\varepsilon$ and 1582 $\mu\varepsilon$, respectively. All of these values are substantially lower than the lower bound of 7000 $\mu\varepsilon$ reported for trabecular failure strain.[1–4] Moreover, the continuous relationship created for accuracy and precision as a

function of image acquisition time and spatial resolution can be used to determine in future studies the choice of measurement spatial resolution and image acquisition time. This will both ensure acceptable levels of measurement accuracy and precision, ameliorate the amount of time it takes to create DVC strain measurements in similar applications and at similar imaging resolutions.

Objective 2 of this thesis work was to quantify the accuracy and precision of DVC-derived strain measurements in scapulae emulating a hemiarthroplasty condition: that is, by being in contact with a material that has the capability to cause significant imaging artifacts. It was found that the DVC-derived strain measurement accuracy and precision at a sub-volume size of 1072 μm were 811 με and 2574 με in the scans containing the CoCr humeral head, and 542 and 534 με in the scans containing the ceramic humeral head. While these values are higher than the values obtained in the first study, they are still substantially lower than the lower bound of trabecular failure strain of 7000 με. [1–4] There was a significant relationship in terms of the measurement error distance from humeral head, with slices containing the humeral head implants having a substantially larger error than those that did not. Also, there is no guarantee that the structural information in these slices was accurate, as the dice correlation coefficient with respect to the reference scapula image in these regions was significantly lower. Based on these observations, DVC derived strain measurements in similar applications and using similar imaging parameters must be wary of the meaningfulness of measurements made in close proximity to artifact-inducing materials. In terms of the CoCr humeral head, measurements made within 1.5mm must be regarded as suspect under the imaging and DVC parameters reported; with the ceramic humeral head measurements made within 1mm must also be scrutinized for error.

The Stewart platform compatible loading fixture designed for the study discussed in Chapter 4 needed to be able to generate displacements that exceeded 0.62 mm in order to be able to simulate eccentric load edge lift off of the glenoid. The loading fixture was able to generate displacements larger than 0.62 mm, with a maximum linear peg displacement of 0.74mm at 4deg of rotational displacement in the primarily tensile based loading. As compressive displacements were thought to be much lower than the tensile

displacements as the glenoid implant likely resists compressive displacement much more effectively due to the presence of bone below the implant, the maximum linear displacement of 0.55mm was thought to be sufficient to simulate peg loading in a primarily compressive loading.

Objective 3 defined goals with respect to the study outlined in Chapter 4: the relationship between maximum and minimum principal strains and certain regions of interest were defined at multiple rotational displacements in bone cores containing glenoid pegs. The relationships hypothesized about the relationship between peg location and strain were found to exist: there was found to be a significant effect of measurement site along the peg and the effect on DVC-measured maximum and minimum principal strains in the cores subjected to primarily tensile loading ($F(3)=7.642$, $p<.001$). The regions close to the surface of the bone core experienced the highest strains, with the strains declining towards the bottom of the peg. However, this relationship was not found to exist in the cores subjected to primarily compressive loading. There was also a significant effect of the sampling region with respect to distance from the peg—regions farther from the peg tended to have lower maximum and minimum principal strains in both the tensile ($F(1)=75.281$, $p<.001$) and compressive-based loading ($F(1)=63.227$, $p<.001$), while regions within 1mm of the peg had higher strains. Interestingly, there was no significant difference between the magnitude of maximum and minimum principal strains.

5.2   Strengths and Limitations

This thesis used a zero-strain assumption to internally assess the accuracy and precision of DVC strain measurements made in cadaveric and recovered tissue samples of the upper extremity. Chapters 2 to 4 all used some form of zero-strain assumption uncertainty analysis to construct a relationship between some parameter of interest (in the case of Chapter 2, both CT projection count and DVC measurement spatial resolution; in Chapters 3 and 4, only DVC spatial resolution). Ideally however, these measures of accuracy and precision would be validated against other methods of determining measurement accuracy and precision. A virtual strain uncertainty analysis, where some known virtual strain is applied to volumetric imagery and the difference between calculated strains and the known strain is assessed, would perhaps refute or confirm the

values of measurement accuracy and precision reported in the zero-strain uncertainty analysis. Nonetheless, Chapter 2 used a form of loaded repeatability analysis to determine the repeatability of strain measurements made of loaded scapulae, which can then be contrasted with the predicted measurement accuracy and precision calculated with the zero-strain uncertainty analysis. As expected, it was found that loaded measurement accuracy and precision as determined through the repeatability analysis were lower than what was predicted through the zero-strain analysis. In the future, best practice would be to include multiple methods of DVC validation: a zero-strain analysis, alongside a virtual strain analysis and a loaded repeatability analysis would all work well in concert with one another and provide a more robust prediction of DVC measurement accuracy and precision. However, the relationships derived for measurement uncertainty in Chapters 2 and 3 as related to parameters of interest are still useful in deciding future DVC and experimental parameters. For example, if investigating the biomechanics of the glenoid implant in the scapula using DVC, an estimate of the measurement uncertainty can be obtained based on the required measurement spatial resolution and imaging parameters used. If investigating the biomechanics of hemiarthroplasties using DVC, it is now known that there is a significant effect of implant-induced artifact on DVC measurements in regions of volumetric imagery closest to the implant, therefore, future investigations must take this effect into account.

The study performed in Chapter 4 used patient-specific humeral osteotomy tissue to model glenoid tissue. There was a significant assumption that trabecular bone on both sides of the glenohumeral interface is similar in terms of material and mechanical properties. As far as the author could find, there were no population studies assessing the bone morphometric parameters of glenoid tissue; if there were, the bone morphometric parameters obtained of the humeral osteotomy tissue could confirm the assumption made in the study—however, as no such data was found, it is an open question whether the materials are similar. Moreover, the cement mixing process, a fundamental aspect of ensuring adequate PMMA bone cement material properties *in vivo*, followed manufacturer instructions but did not emulate aspects of mixing that are incorporated into orthopedic applications such as vacuum mixing.

Another limitation present in Chapters 2 to 4 is the low sample size: in Chapter 2, only two scapulae were investigated. In Chapter 3, only one scapula was investigated under multiple conditions. In Chapter 4, 5 pegs (n=5) were assigned to each experimental group. This is partly a function of the difficulty to source and work with cadaveric material that is relevant to the experimental design; low sample sizes are commonplace in the literature combining cadaveric specimens, volumetric micro-CT imagery and the DVC approach. In the future, increasing this sample size would strengthen the findings here. Moreover, performing parametric analyses so that the results are more generalizable across a range of imaging and DVC parameters would also improve the applicability of the findings of each chapter.

5.3   Future Work

Future studies on the basis of this thesis would likely use the information within to investigate more clinically relevant formulations of the problems discussed within, i.e. using biomechanical loading combined with high resolution volumetric imagery and DVC to investigate critical interfaces within the glenohumeral joint. Measurement accuracy and precision concerns would be secondary to the investigation of the problems themselves and serve to inform the primary findings instead of being the primary focus of the studies. To that end, a logical continuation of the findings of Chapter 2 would be to incorporate multiple load vectors that are representative of what is experienced *in vivo* and observe the mechanical response of the glenoid implant and the implant-bone-cement interface beneath using DVC. This could also be extended to Chapter 3: the incorporation of multiple load vectors, alongside a comparison of multiple hemiarthroplasty implant material offerings and the strain pattern underneath the glenoid could shed light on the clinical question of glenoid erosion in hemiarthroplasty.

Another avenue of investigation to continue the work here is to incorporate cyclic loading into the loading protocols. *In vivo* failure of glenoid implants in TSA and glenoid erosion in SHA are thought to be strongly dependent on the many thousands of loading cycles experienced by the shoulder joint during normal ambulation. Perhaps the use of cyclic loading in combination with DVC can shed light on the degradation of the interface as a function of loading cycles. There is a practical difficulty here, however, as cyclic loading

is highly time-dependent and concerns with cadaveric longevity outside of a preservative environment might be detrimental to the overall feasibility of the experimental design. It still may be possible in some way, but an understanding of the degradation of the mechanical properties of cadaveric tissue over time outside of a preservative environment are critical to tempering the results of such a study.

As in Chapter 4, other routes of study could be to examine specific sub-elements of interest of these clinical problems. The high resolution of imagery involved in a DVC measurement enables clinical problems to be sub-divided into smaller investigations; understanding how the initiation of microscopic failure translates into macroscopic failure is the open question in some of these clinical problems and a DVC approach can begin to probe that area of knowledge translation.

5.4 Thesis Conclusion

The combination of digital volume correlation and high-resolution volumetric imagery enables the precision study of open clinical problems in the osteoarthritic glenohumeral joint. The accuracy and precision of this experimental approach is assessed in the context of medical implants and materials typically used in these applications, and key findings about the nature of measurement uncertainty in the presence of these materials were elucidated. Moreover, knowledge derived from the previous studies of measurement uncertainty were translated to an analysis of a critical region of failure in the glenoid implant-cement-bone interface, which demonstrates the feasibility of the DVC approach to investigate the clinical problems of osteoarthritic glenohumeral joint. The findings of this thesis contribute to the body of knowledge surrounding the application of digital volume correlation in the upper extremity through the integration of biomechanical testing, high resolution CT imagery and digital volume correlation measurements derived thereof.

5.5   References

1.   Morgan EF, Keaveny TM. Dependence of yield strain of human trabecular bone on anatomic site. *Journal of Biomechanics*. 2001;34(5):569-577. doi:10.1016/S0021-9290(01)00011-2

2.   Odgaard A, Hvid I, Linde F. Compressive axial strain distributions in cancellous bone specimens. *Journal of Biomechanics*. 1989;22(8-9):829-835. doi:10.1016/0021-9290(89)90066-3

3.   Bayraktar HH, Morgan EF, Niebur GL, Morris GE, Wong EK, Keaveny TM. Comparison of the elastic and yield properties of human femoral trabecular and cortical bone tissue. *Journal of Biomechanics*. 2004;37(1):27-35. doi:10.1016/S0021-9290(03)00257-4

4.   Nagaraja S, Couse TL, Guldberg RE. Trabecular bone microdamage and microstructural stresses under uniaxial compression. *Journal of Biomechanics*. 2005;38(4):707-716. doi:10.1016/J.JBIOMECH.2004.05.013

Appendix A: Uncertainty Analysis of Pegged Bone Core Constructs

OVERVIEW

In order to have a gauge on the level of measurement accuracy and precision in an given digital volume correlation workflow an uncertainty analysis must be performed. For the study outlined in Chapter 4, the uncertainty analysis was not critical to the outcome being investigated but rather a necessary control step to identify the measurement uncertainties associated with the DVC methodology applied. This appendix contains the zero-strain uncertainty analysis performed on the bone cores used in Chapter 4 in order to quantify the DVC measurement accuracy and precision of the workflow used.
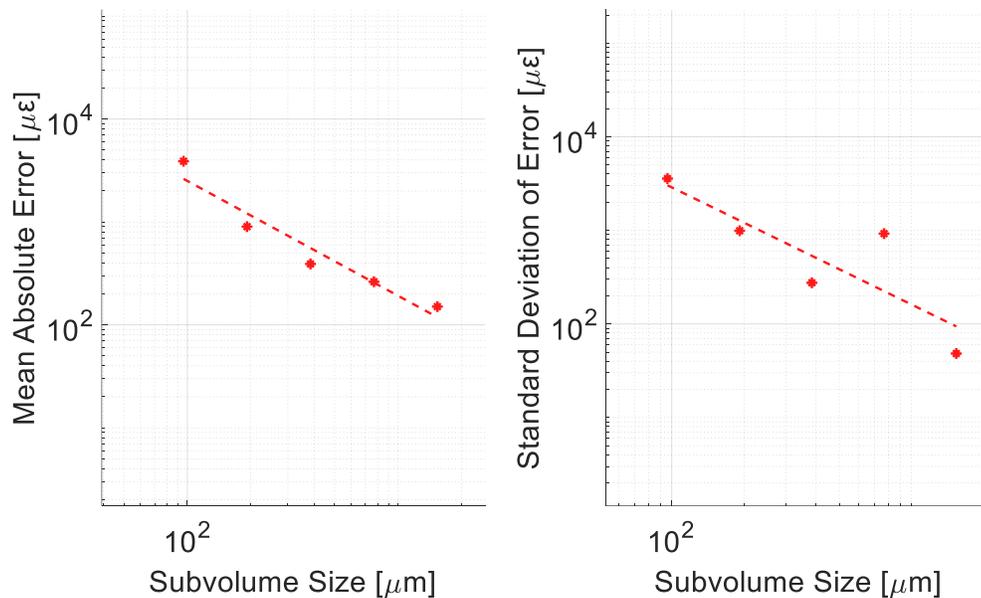
Figure 24: Mean absolute error and standard deviation of error in the uncertainty analysis performed on the bone core-peg constructs.

Table 9: Peg-bone core construct uncertainty analysis data presented in tabular form

Sub-volume Size [μm]	Mean Absolute Error [με]	Standard Deviation of Error [με]
96	3889	3577
192	900	991
384	391	275
768	262	924
1536	15	48

Appendix B: Matlab® Scripts used to Analyze DVC Results

OVERVIEW

This appendix contains the Matlab® scripts used in Chapters 2 to 4. The first script was used to calculate the mean absolute error and standard deviation of error in the unloaded uncertainty analysis performed in Chapter 2, 3 and 4. The second script was used to calculate the mean relative difference in apparent strain and standard deviation of the apparent strain used in the loaded repeatability analysis performed in Chapter 2.

B.1-Mean Absolute Error and Standard Deviation of Error

This script accepts 6 .tp files corresponding to each element of the sub-volume strain tensors for the DVC analyses performed at each investigated level of spatial resolution and CT projection count. The output is a matrix containing the mean absolute error and standard deviation of error at each investigated level.

```
% UNCERTAINTY ANAYLSIS REVISION 3
% CONSTRUCTS "data" VARIABLE CONTAINING GLOBAL MAE AND SDE OF ALL POPULATED
STRAIN
% TENSORS FOR VARIED DVC NODAL SPACING AND OPTIONALLY VARIED SCAN DURATION


%THESE TWO VARIABLES ARE THE EXTERNAL INTERFACE TO THE SCRIPT, CHANGE
%THESE BEFORE CHANGING OTHER STUFF
%t_incre is an optional arbitrary length vector typically containing
%different scan lengths
%n_spacing_incre is a required arbitrary length vector containing the nodal
%spacing parameters thats the digital volume correlation was performed at
t_incre=[3,6,15,30,60];
n_spacing_incre=[8,16,32,64,128];



m=length(t_incre);
n=length(n_spacing_incre);

%"data" structured s.t. there are n rows (equal to the number of different
nodal
%spacings) with an extra row of padding containing column headers and 3*m
%columns containing the optional different scan time MAERs and SDERs
data=zeros(n+1,m*3);


%directory of data relative to script position, under the assumption that
%the rest of the directory format below is correct--its useful to maintain
```

```matlab
%same format so maybe structure them as below in LaVis for continuity
%AS OF LAVISION 10.1.1 Export structure has changed--file format specifier
%must change as well
root_dir="Data 06.16.20/Keel Unloaded";
%N__Keel Unloaded_Kusins_UncertaintyAnalysis_No Load_%d_%dNodal_%s20002
%O__Jakub-DVC Workspace_Jakub_UA_Peg_Jakub_UA_Peg_Unloaded-%d_%dNodal_%s20002
tic


for i=1:m
    for j=1:n

        Exxfile=sprintf('%s/%s/N__Keel Unloaded_Kusins_UncertaintyAnalysis_No
Load_%d_%dNodal_%s20002.dat',root_dir,'Exx',t_incre(i),
n_spacing_incre(j),'Exx');
        Exx=importdata(Exxfile);
        Exx=Exx.data(:,1:5);

        Exyfile=sprintf('%s/%s/N__Keel Unloaded_Kusins_UncertaintyAnalysis_No
Load_%d_%dNodal_%s20002.dat',root_dir,'Exy', t_incre(i),
n_spacing_incre(j),'Exy');
        Exy=importdata(Exyfile);
        Exy=Exy.data(:,1:5);

        Exzfile=sprintf('%s/%s/N__Keel Unloaded_Kusins_UncertaintyAnalysis_No
Load_%d_%dNodal_%s20002.dat',root_dir,'Exz', t_incre(i),
n_spacing_incre(j),'Exz');
        Exz=importdata(Exzfile);
        Exz=Exz.data(:,1:5);

        Eyyfile=sprintf('%s/%s/N__Keel Unloaded_Kusins_UncertaintyAnalysis_No
Load_%d_%dNodal_%s20002.dat',root_dir,'Eyy', t_incre(i),
n_spacing_incre(j),'Eyy');
        Eyy=importdata(Eyyfile);
        Eyy=Eyy.data(:,1:5);

        Eyzfile=sprintf('%s/%s/N__Keel Unloaded_Kusins_UncertaintyAnalysis_No
Load_%d_%dNodal_%s20002.dat',root_dir,'Eyz', t_incre(i),
n_spacing_incre(j),'Eyz');
        Eyz=importdata(Eyzfile);
        Eyz=Eyz.data(:,1:5);

        Ezzfile=sprintf('%s/%s/N__Keel Unloaded_Kusins_UncertaintyAnalysis_No
Load_%d_%dNodal_%s20002.dat',root_dir,'Ezz', t_incre(i),
n_spacing_incre(j),'Ezz');
        Ezz=importdata(Ezzfile);
        Ezz=Ezz.data(:,1:5);

        %possibly a repetition of whats conducted below--this one seems
        %less robust--assumes that if strain field is 0 for one must be
        %zero for others... probably remove this one
        nz_ind=find(Exx(:,4));

        Exx=Exx(nz_ind,:);
        Exy=Exy(nz_ind,:);
```

```
        Exz=Exz(nz_ind,:);
        Eyy=Eyy(nz_ind,:);
        Eyz=Eyz(nz_ind,:);
        Ezz=Ezz(nz_ind,:);

        SExx=gpuArray(Exx(:,4));
        SExy=gpuArray(Exy(:,4));
        SExz=gpuArray(Exz(:,4));
        SEyy=gpuArray(Eyy(:,4));
        SEyz=gpuArray(Eyz(:,4));
        SEzz=gpuArray(Ezz(:,4));


        %seperate nonzero values and resize array--(possibly a repeated
        %step? maybe delete this)
        SExx(SExx==0)=[];
        SExy(SExy==0)=[];
        SExz(SExz==0)=[];
        SEyy(SEyy==0)=[];
        SEyz(SEyz==0)=[];
        SEzz(SEzz==0)=[];


        %absolute values of each array
        SExx=abs(SExx);
        SExy=abs(SExy);
        SExz=abs(SExz);
        SEyy=abs(SEyy);
        SEyz=abs(SEyz);
        SEzz=abs(SEzz);



        abs_val=[SExx SExy SExz SEyy SEyz SEzz];
        abs_val=abs_val*1e6;
        avg=mean(abs_val,2);
        MAER=mean(avg);
        norm=avg-MAER;

        sq=norm.^2;
        SDER=sqrt(mean(sq));

        MAER=gather(MAER);
        SDER=gather(SDER);


        data(1, 1+3*(i-1))=t_incre(i);
        data(1+j, 1+3*(i-1))=n_spacing_incre(j);
        data(1+j, 2+3*(i-1))=MAER;
        data(1+j, 3+3*(i-1))=SDER;

    end
  i
end
toc
```

B.2-Mean Relative Difference of Strain and Standard Deviation of the Difference in Strain

This script accepts 6 .tp files corresponding to each element of the sub-volume strain tensors for the DVC analyses performed at each investigated level of CT projection count for a loaded repeatability analysis. The output is a matrix containing the mean relative difference in strain and the strain deviation of the difference in strain as a function of CT projection count.

```matlab
t_incre=[3,6,15,30,60];
n_spacing_incre=[32];


m=length(t_incre);
n=length(n_spacing_incre);

.dat'
data=zeros(17,m*n);
for i=1:n
    dat=importdata(sprintf('Data 07.30.20/Keel Loaded/%s/O__Jakub-DVC
Workspace_Jakub_UA_Keel_Keel-%d-Load-
Registered_%dNodal_%s20002.dat','Exx',60,32,'Exx'));
    size_test=dat.data;
    sz=length(size_test);

    iexx=zeros(sz,5);
    iexy=zeros(sz,5);
    iexz=zeros(sz,5);
    ieyy=zeros(sz,5);
    ieyz=zeros(sz,5);
    iezz=zeros(sz,5);

    for j=1:m
        sprintf('Data 07.30.20/Keel Loaded/%s/O__Jakub-DVC
Workspace_Jakub_UA_Keel_Keel-%d-Load-Registered_%dNodal_%s20002.dat','Exx',
t_incre(j),n_spacing_incre(i),'Exx')
        exx_dat=importdata(sprintf('Data 07.30.20/Keel Loaded/%s/O__Jakub-DVC
Workspace_Jakub_UA_Keel_Keel-%d-Load-Registered_%dNodal_%s20002.dat','Exx',
t_incre(j),n_spacing_incre(i),'Exx'));
        exy_dat=importdata(sprintf('Data 07.30.20/Keel Loaded/%s/O__Jakub-DVC
Workspace_Jakub_UA_Keel_Keel-%d-Load-Registered_%dNodal_%s20002.dat','Exy',
t_incre(j),n_spacing_incre(i),'Exy'));
        exz_dat=importdata(sprintf('Data 07.30.20/Keel Loaded/%s/O__Jakub-DVC
Workspace_Jakub_UA_Keel_Keel-%d-Load-Registered_%dNodal_%s20002.dat','Exz',
t_incre(j),n_spacing_incre(i),'Exz'));
        eyy_dat=importdata(sprintf('Data 07.30.20/Keel Loaded/%s/O__Jakub-DVC
Workspace_Jakub_UA_Keel_Keel-%d-Load-Registered_%dNodal_%s20002.dat','Eyy',
t_incre(j),n_spacing_incre(i),'Eyy'));
```

```matlab
        eyz_dat=importdata(sprintf('Data 07.30.20/Keel Loaded/%s/O__Jakub-DVC
Workspace_Jakub_UA_Keel_Keel-%d-Load-Registered_%dNodal_%s20002.dat','Eyz',
t_incre(j),n_spacing_incre(i),'Eyz'));
        ezz_dat=importdata(sprintf('Data 07.30.20/Keel Loaded/%s/O__Jakub-DVC
Workspace_Jakub_UA_Keel_Keel-%d-Load-Registered_%dNodal_%s20002.dat','Ezz',
t_incre(j),n_spacing_incre(i),'Ezz'));

        exx=exx_dat.data;
        exy=exy_dat.data;
        exz=exz_dat.data;
        eyy=eyy_dat.data;
        eyz=eyz_dat.data;
        ezz=ezz_dat.data;

        iexx(:,j)=exx(:,4);
        iexy(:,j)=exy(:,4);
        iexz(:,j)=exz(:,4);
        ieyy(:,j)=eyy(:,4);
        ieyz(:,j)=eyz(:,4);
        iezz(:,j)=ezz(:,4);

    end


    num=length(iexx);

    dataexx=zeros(num,5);
    dataexy=zeros(num,5);
    dataexz=zeros(num,5);
    dataeyy=zeros(num,5);
    dataeyz=zeros(num,5);
    dataezz=zeros(num,5);

    rev_exx_dat=importdata(sprintf('Data 07.30.20/Keel Loaded/%s/O__Jakub-DVC
Workspace_Jakub_UA_Keel_Keel-%d-Load-2-Registered_%dNodal_%s20002.dat','Exx',
60,32,'Exx'));
    rev_exy_dat=importdata(sprintf('Data 07.30.20/Keel Loaded/%s/O__Jakub-DVC
Workspace_Jakub_UA_Keel_Keel-%d-Load-2-Registered_%dNodal_%s20002.dat','Exy',
60,32,'Exy'));
    rev_exz_dat=importdata(sprintf('Data 07.30.20/Keel Loaded/%s/O__Jakub-DVC
Workspace_Jakub_UA_Keel_Keel-%d-Load-2-Registered_%dNodal_%s20002.dat','Exz',
60,32,'Exz'));
    rev_eyy_dat=importdata(sprintf('Data 07.30.20/Keel Loaded/%s/O__Jakub-DVC
Workspace_Jakub_UA_Keel_Keel-%d-Load-2-Registered_%dNodal_%s20002.dat','Eyy',
60,32,'Eyy'));
    rev_eyz_dat=importdata(sprintf('Data 07.30.20/Keel Loaded/%s/O__Jakub-DVC
Workspace_Jakub_UA_Keel_Keel-%d-Load-2-Registered_%dNodal_%s20002.dat','Eyz',
60,32,'Eyz'));
    rev_ezz_dat=importdata(sprintf('Data 07.30.20/Keel Loaded/%s/O__Jakub-DVC
Workspace_Jakub_UA_Keel_Keel-%d-Load-2-Registered_%dNodal_%s20002.dat','Ezz',
60,32,'Ezz'));


    rev_exx=rev_exx_dat.data;
    rev_exy=rev_exy_dat.data;
```

```
rev_exz=rev_exz_dat.data;
rev_eyy=rev_eyy_dat.data;
rev_eyz=rev_eyz_dat.data;
rev_ezz=rev_ezz_dat.data;



for j=1:m
    if j==1
        dataexx(:,j)=iexx(:,5)-rev_exx(:,4);
        dataexy(:,j)=iexy(:,5)-rev_exy(:,4);
        dataexz(:,j)=iexz(:,5)-rev_exz(:,4);
        dataeyy(:,j)=ieyy(:,5)-rev_eyy(:,4);
        dataeyz(:,j)=ieyz(:,5)-rev_eyz(:,4);
        dataezz(:,j)=iezz(:,5)-rev_ezz(:,4);
    else
        dataexx(:,j)=iexx(:,5-(j-1))-iexx(:,5);
        dataexy(:,j)=iexy(:,5-(j-1))-iexy(:,5);
        dataexz(:,j)=iexz(:,5-(j-1))-iexz(:,5);
        dataeyy(:,j)=ieyy(:,5-(j-1))-ieyy(:,5);
        dataeyz(:,j)=ieyz(:,5-(j-1))-ieyz(:,5);
        dataezz(:,j)=iezz(:,5-(j-1))-iezz(:,5);
    end


end

dataexx=dataexx.*1e6;
dataexy=dataexy.*1e6;
dataexz=dataexz.*1e6;
dataeyy=dataeyy.*1e6;
dataeyz=dataeyz.*1e6;
dataezz=dataezz.*1e6;

dataexx=abs(dataexx);
dataexy=abs(dataexy);
dataexz=abs(dataexz);
dataeyy=abs(dataeyy);
dataeyz=abs(dataeyz);
dataezz=abs(dataezz);

dataexx = dataexx(any(dataexx,2),:);
dataexy = dataexy(any(dataexy,2),:);
dataexz = dataexz(any(dataexz,2),:);
dataeyy = dataeyy(any(dataeyy,2),:);
dataeyz = dataeyz(any(dataeyz,2),:);
dataezz = dataezz(any(dataezz,2),:);

meanexx=mean(dataexx);
meanexy=mean(dataexy);
meanexz=mean(dataexz);
meaneyy=mean(dataeyy);
meaneyz=mean(dataeyz);
meanezz=mean(dataezz);
```

```
    stdexx=std(dataexx);
    stdexy=std(dataexy);
    stdexz=std(dataexz);
    stdeyy=std(dataeyy);
    stdeyz=std(dataeyz);
    stdezz=std(dataezz);

    mean_vec=[meanexx; meanexy; meanexz; meaneyy; meaneyz; meanezz];
    std_vec=[stdexx; stdexy; stdexz; stdeyy; stdeyz; stdezz];

    mean_rel_diff=mean(mean_vec);
    mean_std_rel_diff=mean(std_vec);

    data(1,1+m*(i-1))=n_spacing_incre(i);
    data(2,1+m*(i-1):m+m*(i-1))=flip(t_incre);
    data(3:9,1+(m*(i-1)):m+m*(i-1))=[meanexx; meanexy; meanexz; meaneyy;
meaneyz; meanezz; mean_rel_diff];
    data(10,1+m*(i-1):m+m*(i-1))=flip(t_incre);
    data(11:17,1+(m*(i-1)):m+m*(i-1))=[stdexx; stdexy; stdexz; stdeyy; stdeyz;
stdezz; mean_std_rel_diff];
end
```

Curriculum Vitae

Name:	Jakub Robert Targosinski
Post-secondary Education and Degrees:	University of Toronto Toronto, Ontario, Canada 2014-2019 B.A.Sc.
Honours and Awards:	Governor General's Academic Bronze Medal 2014 CMHR Graduate Trainee 2021 MITACS Accelerate Internship 2022
Related Work Experience	Teaching Assistant The University of Western Ontario 2020-2021

Publications: (n=2)

(accepted for publication) Targosinski J, Kusins J, Martensson N, Nelson A, Knowles N, Ferreira L. Assessing Methodological Uncertainty of In-Vitro Digital Volume Correlation Bone Strain Measurements in Total Shoulder Arthroplasties. Lecture Notes in Computational Vision and Biomechanics. **(2022)**

Kusins J, Knowles N, Targosinski J, Columbus M, Athwal G, Ferreira L. 3D Strain Analysis of Osteoarthritic Trabecular Bone within the Humeral Head Subjected to Stepwise Compressive Loads. Journal of the Mechanical Behavior of Biomedical Materials. Vol 125. **(Jan. 2022)**

Research Posters: (n=2)

Targosinski J, Kusins J, Martensson N, Nelson A, Knowles N, Ferreira L. Assessing Methodological Uncertainty of In-Vitro Digital Volume Correlation Bone Strain Measurements in Total Shoulder Arthroplasties. 17th International Symposium on Computer Methods in Biomechanics and Biomedical Engineering and the 5th Conference on Imaging and Visualization **(2021, Poster)**

Kusins J, Knowles N, Targosinski J, Columbus M, Athwal G, Ferreira L. 3D Strain Analysis of Osteoarthritic Trabecular Bone within the Humeral Head Subjected to Stepwise Compressive Loads. The 2021 Canadian Orthopaedic Research Society Annual Meeting. **(2021, Poster)**